The Journal of Chemical Physics

Structure and dynamics in suspensions of soft core-shell colloids in the fluid regime

Cite as: J. Chem. Phys. **151**, 024901 (2019); https://doi.org/10.1063/1.5091845
Submitted: 06 February 2019 . Accepted: 17 June 2019 . Published Online: 12 July 2019

Andreas Pamvouxoglou, Panagiota Bogri, Gerhard Nägele, Kohji Ohno, and George Petekidis

View Online Export Citation CrossMark

ARTICLES YOU MAY BE INTERESTED IN

Ohm's law for ion conduction in lithium and beyond-lithium battery electrolytes
The Journal of Chemical Physics **151**, 020901 (2019); https://doi.org/10.1063/1.5109684

Efficient dynamic simulations of charged dielectric colloids through a novel hybrid method
The Journal of Chemical Physics **151**, 024112 (2019); https://doi.org/10.1063/1.5110628

Ions' motion in water
The Journal of Chemical Physics **150**, 190901 (2019); https://doi.org/10.1063/1.5090765

AIP Publishing

The Journal of Chemical Physics ARTICLE scitation.org/journal/jcp

Structure and dynamics in suspensions of soft core-shell colloids in the fluid regime

Cite as: J. Chem. Phys. 151, 024901 (2019); doi: 10.1063/1.5091845
Submitted: 6 February 2019 • Accepted: 17 June 2019 •
Published Online: 12 July 2019

Andreas Pamvouxoglou,[1,a)] **Panagiota Bogri,**[1] **Gerhard Nägele,**[2] **Kohji Ohno,**[3] **and George Petekidis**[1,b)]

AFFILIATIONS

[1] FORTH-IESL and Department of Materials Science and Technology, University of Crete, 71110, Heraklion, Crete, Greece
[2] Forschungszentrum Jülich GmbH, ICS-3 - Soft Condensed Matter, 52428 Jülich, Germany
[3] Institute for Chemical Research, Kyoto University, Uji, Kyoto 611-0011, Japan

[a)] **Present address:** Experimental Soft Matter Group, Condensed Matter Physics Laboratory (IPKM), Heinrich Heine University, Universitätsstrasse 1, 40225, Düsseldorf, Germany.
[b)] **Electronic mail:** georgp@iesl.forth.gr.

ABSTRACT

We report on a detailed experimental study of the structure and short-time dynamics in fluid-regime suspensions of soft core-shell spherical particles with different molecular weights of the chains forming the soft outer shell, and therefore different degrees of particle softness, using 3D dynamic light scattering (3D-DLS). Owing to the particle softness, the liquid-crystal coexistence regime is found to be broader than that of hard-sphere (HS) suspensions. Static light scattering in the dilute regime yields form factors that can be described using a spherical core-shell model and second virial coefficients $A_2 > 0$ indicative of purely repulsive interactions. The particle-particle interactions are longer ranged for all considered systems except those of the smaller molecular weight chain grafted particles which show a HS-like behavior. 3D-DLS experiments in the concentrated regime up to the liquid-crystal transition provide the short-time diffusion function, $D(q)$, in a broad range of scattering wavenumbers, q, from which the structural (cage) and short-time self-diffusion coefficients $D(q_m)$ and $D_S = D(q \gg q_m)$, respectively, are deduced as functions of the effective particle volume fraction, $\phi = c/c^*$, where c^* is the overlap concentration, calculated using the hydrodynamic particle radius, R_H. The size of the nearest-neighbor cage of particles is characterized by $2\pi/q_m$, with $D(q)$ and the static structure factor $S(q)$ attaining at q_m the smallest and largest values, respectively. Experimental data of $D(q_m)$ and D_S are contrasted with analytic theoretical predictions based on a simplifying hydrodynamic radius model where the internal hydrodynamic structure of the core-shell particles is mapped on a single hydrodynamic radius parameter $\gamma = R_H/R_{eff}$, for constant direct interactions characterized by an (effective) hard-core radius R_{eff}. The particle softness is reflected, in particular, in the corresponding shape of the static structure factor, while the mean solvent (Darcy) permeability of the particles related to γ is reflected in the dynamic properties only. For grafted particles with longer polymer chains, $D(q_m)$ and D_S are indicative of larger permeability values while particles with shorter chains are practically nonpermeable. The particle softness is also evident in the effective random close packing fraction estimated from the extrapolated zero-value limit of the cage diffusion coefficient $D(q_m)$.

I. INTRODUCTION

Solutions of homopolymer chains and suspensions of rigid colloidal particles are two important classes of soft matter systems. While to a certain extent they behave similarly in the liquid phase regime, their detailed dynamics in concentrated systems is quite different, as reflected by the different hydrodynamic interactions (HIs) mediated by the associated local solvent flow pattern. Different from rigid colloidal particles which typically are solvent-impermeable, the flexible polymer coils are solvent permeable under good solvent conditions. While the HIs between mobile colloids in the fluid phase are nonscreened, in concentrated polymer solutions with concentrations c above the overlap concentration c^*, there is hydrodynamic screening operative owing to the (transient) formation of interchain and intrachain entanglement contacts.[1] There is thus a distinctly different concentration dependence of diffusion and viscoelastic properties dictated by the different strength and range of the HIs.[2–10]

Understanding the effect of HIs in dispersions of composite particles of intermediate character such as polymer grafted colloids or soft core-shell particles is still a largely open issue, providing a good motivation for experimental studies using well-characterized model systems. Well-studied systems with intermediate colloid-polymer properties are microgel particles,[7,10–14] multiarm starlike polymers or micelles, and core-shell particles with either a crosslinked polymer shell or dense grafted polymer chains. By varying the number of grafted polymer chains (or polymer arms) or the amount of crosslinking, the system behavior can be changed from that of nearly rigid colloidal particles to that of soft repulsive colloids (when highly grafted small polymer chains are used) and eventually to that of dispersions where the ultrasoft polymer chain dynamics dominates (for example, in the case of high-molecular-weight grafted polymer chains).[6,9,15] Recently, Gupta *et al.*[16] studied the phase behavior of soft copolymers in order to establish a generalized phase diagram used in turn to investigate the microstructural influence on the equilibrium dynamics of soft colloids. Based on a simple coarse-grained model for the interparticle interaction potential, they determined an interaction length and presented a quantitative comparison between theory and experiment.

For hard-sphere (HS) suspensions, the self-diffusion dynamics both at short and long times slows down with increasing volume fraction, with the long-time self-diffusion coefficient D_L becoming practically zero at a glass transition point and the short-time coefficient D_S vanishing at random close packing (RCP). The decrease in the short-time self-diffusion coefficient D_S with increasing volume fraction has been quantified by Stokesian Dynamics (SD) simulations of Brownian hard spheres by Banchio and Brady[17] up to volume concentrations approaching the random close packing volume fraction $\phi \approx 0.644$ of monodisperse spheres. The coefficient D_S is the large wavenumber limit of the short-time diffusion function $D(q)$ routinely probed in dynamic light scattering (DLS) experiments as a function of the scattering wavenumber $q = (4\pi\nu/\lambda)\sin(\theta/2)$ with ν as the optical refractive index of the medium, λ as the wavelength of the laser light in vacuum, and θ as the scattering angle. At larger concentrations, $D(q)$ significantly deviates from the single-particle diffusion coefficient D_0, reflecting thus the combined effects of the equilibrium structure and HIs on short-time collective diffusion across a distance $\sim 2\pi/q$. DLS results for the $D(q)$ of colloidal hard spheres are discussed, e.g., in Refs. 18 and 19. Owing to the "stiffness" of the nearest-neighbor cage formed around each particle, $D(q)$ is smallest at $q = q_m$. The appearance of a distinct slowing-down of $D(q)$ near the principal peak position, q_m, of $S(q)$ was likewise reported for suspensions of rigid charge-stabilized colloidal particles.[8] The direct interactions in these lower-salinity suspensions can be described by a soft repulsive interparticle potential of Yukawa type, and dynamic properties such as $D(q)$ can be accurately predicted in theory and SD simulation on basis of this effective pair potential, provided the salient HIs are accounted for.[8,20,21] The suspensions of the nonionic microgel particles studied by Eckert and Richtering[7] show a strong slowing down of collective dynamics around q_m that is reminiscent of rigid particles' suspensions, despite the fuzzy character of the microgel surfaces. For the ionic PNiPAM microgel suspensions studied by Holmqvist *et al.*,[22] a dip in $D(q)$ at q_m was likewise observed which deepens with decreasing temperature T and increasing concentration. Moreover, for the surfactant micelles examined by Imai *et al.*[23] that are comprised of a hard core and a weak longer-ranged repulsive potential, a strong slowing down effect on $D(q_m)$ was observed in the fluid phase regime. Core-shell particle suspensions investigated by Petekidis *et al.*[4] exhibit a weaker slowing down of collective diffusion at q_m mainly due to the lower $D(q)$ detected at $q < q_m$. On the other hand, although a study of giant PS-PI diblock micelles by Sigel *et al.*[3] suggested that there is no slowing down of $D(q)$ around q_m, with the average relaxation time from the DLS experiments' field correlation function determined via inverse Laplace transform (based on CONTIN program analysis), careful analysis of the initial slope of the correlation functions does yield a clear slowing down around $D(q_m)$, similar to all other studies of soft and hard colloidal particles. More recently, Riest *et al.*[10] reported an easy-to-use analytic set of methods for calculating short- and long-time dynamic properties of suspensions of nonionic microgel particles with intrinsic hydrodynamic structure, based on the hydrodynamic radius model (HRM). The theoretical predictions for $D(q)$ by this set capture quantitatively the experimental results for nonionic PNIPAM microgels.[7] The suspensions of the soft polymer-grafted colloidal spheres studied by Voudouris *et al.*[9] exhibit structural and dynamic properties close to those of colloidal hard spheres when the polymer chains are short, while for long grafted polymer chains there are significant deviations from the hard-sphere behavior.

In this paper, we investigate the effect of particle softness and solvent permeability on the structure and dynamics of core-shell particle composites dispersed in organic solvents, with the particles consisting of a spherical silica (SiP) core and a shell of highly grafted polymethylmethacrylate (PMMA) polymer chains. We vary the particle softness and solvent permeability by changing the molecular weight of the grafted chains, while keeping nearly constant the surface grafting density and the core size. We compare and discuss the results for $S(q)$ and $D(q)$ obtained by static and dynamic light scattering with results obtained by the 3D dynamic light scattering (3D-DLS) setup to suppress residual multiple scattering at larger concentrations. The experimental data for $D(q)$ are confronted with analytic theoretical results based on the simplifying HRM model where the internal (core-shell) hydrodynamic particle structure is mapped on a single hydrodynamic radius parameter γ treated as the only dynamic fitting parameter from which the mean Darcy permeability of the particles is inferred. On treating the core-shell particles as effective hard spheres regarding their direct interactions and thus regarding $S(q)$, which is an oversimplification for extended polymer shells, we take advantage of analytic expressions for $D(q_m)$, $D(q = 0)$, and D_S as functions of γ and effective volume fraction ϕ_{eff}.

II. METHODS AND SYSTEMS

A. Materials

Hybrid core-shell particles (PMMA-SiPs) with a spherical silica (SiP) core and a shell of grafted polymethylmethacrylate (PMMA) polymer chains were synthesized by surface-initiated atom transfer radical polymerization (ATRP) of MMA, as reported previously.[24] The mean diameter of the silica (SiP) core is 130 nm with a relative standard deviation of 10%, as measured by transmission electron microscopy. The weight-averaged molecular weight (M_w) of the PMMA polymer chains is 41 kg/mol for sample *P2_41k*, 126 kg/mol for sample *P2_126k*, and 402 kg/mol for *P2_402k*, with polydispersity indices (PDIs) 1.25, 1.24, and 1.15, respectively. The surface grafting density of the PMMA chains on the silica core, σ_0, varies between 0.55 and 0.65 chains/nm^2, corresponding about 34 500 grafted chains per particle.

Owing to the high σ_0, two shell regions can be distinguished: (1) a concentrated polymer brush (CPB) regime in which polymer chains are stretched and (2) an intermediate brush region semidilute polymer brush (SDPB) of lower polymer density with less stretched polymer conformations (see Fig. 1). Since for spherical particle brushes the effective polymer density decreases with increasing distance r from the particle center according to $\sigma_{eff} = \sigma_0 (R_C/r)^2$, where R_C denotes the particle core radius, a transition from the concentrated to the semidilute polymer solution regime is expected at a critical distance R_{DC}. This follows from the Daoud-Cotton model for star polymers according to which $R_{DC} = 2 \upsilon R_C (\pi \sigma^*)^{0.5}$, with $\sigma^* = \sigma_0 \alpha^2$ denoting the dimensionless surface coverage (α is the monomer length) and υ denoting the Flory-Huggins excluded-volume parameter that is approximately equal to b/α, with b as the Kuhn segment length for an athermal solvent.[25] For f chains grafted to the surface of the silica core, $\sigma_0 = f/\left(4\pi R_C^2\right)$ and $R_{DC} \approx b f^{0.5}$ is the radius of the core plus CPB region where for the latter, excluded-volume effects are screened out. The ratio R_C/L, with $L = R_N/\sqrt{6}$ and R_N as the mean polymer end-to-end distance in a good solvent, can serve as a measure for the softness of the core-shell particles which varies depending on the polymer molecular weight and the solvent quality. The theoretical overall particle size can be estimated from $R_{tot} = R_C + L$. Experimentally, R_{tot} can be determined as the hydrodynamic radius, R_H, measured by Dynamic Light Scattering (DLS), or from Static Light Scattering (SLS), denoted then as R_{SLS}.

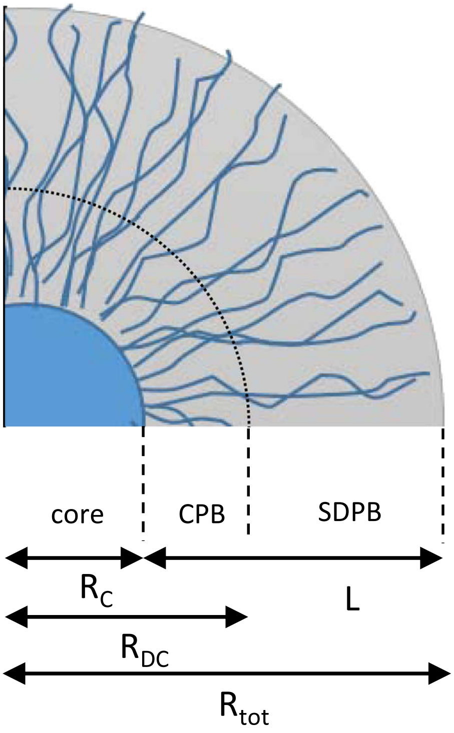

FIG. 1. Schematics of the core-shell hybrid particle cross section showing the two polymer brush regions. In the concentrated polymer brush region (CPB), chains are stretched due to excluded volume effects, while in the semidilute polymer brush region (SDPB) of thickness *L* the chain conformations change with increasing distance from the core, from nearly fully stretched chains to coiled chains of nearly Gaussian conformation.

To achieve particle-solvent refractive index matching as required in order to suppress multiple scattering, we used different solvent mixtures. Specifically, we used 50%–50% (by volume) of 1, 2-dichloroethane (DE) and *o*-dichlorobenzene (DCB) for *P2_126k*, while a mixture of *o*-dimethoxy benzene (veratrole) and dimethyl formamide (DMF) was used for *P2_41k* and *P2_402k* to index match the PMMA shell with optical refractive index $\nu_s = 1.489$ at laser wavelength $\lambda = 633$ nm. For comparison, *P2_402k* particles were also dispersed in toluene which is known to be a good solvent for PMMA polymer chains. The effective densities of the particles were calculated based on the volume weighted density of the core, PMMA, and solvent using the equation $d_{eff} = (d_c V_c + d_{PMMA} V_{PMMA} + d_0 V_0)/(4/3)\pi R_H^3$, where *c* denotes the silica core, *PMMA* denotes the PMMA chains, and *0* denotes the solvent. The calculated d_{eff} are 1.16, 1.28, 1.04, and 0.88 g/ml for *P2_41k* in Ver-DMF, *P2_126k* in DCB-DE, *P2_402k* in Ver-DMF, and *P2_402k* in toluene, respectively.

In order to determine the phase diagram of these systems, we prepared different suspensions in square cells of 4 mm thickness. Samples were kept at constant room temperature for two days before visual observation (see the middle panel of Fig. 2). The bottom panel of Fig. 2 shows the schematic phase diagram for the intermediate size core-shell, *P2_126k*, particles dispersed in DCB-DE as a function of volume fraction, ϕ, deduced from the direct observation, where liquid, liquid-crystal coexistence, and a fully crystalline phase (mixture of FCC and HCP) are indicated. In practice, the samples were prepared by mixing appropriate weight of solvent and polymer; therefore, the concentration, c, was determined in weight/weight (wt. %) and was compared with the corresponding overlap concentration. Although the concentration (in wt. %) or the number density (number of particles per volume) is unambiguously defined, none of these quantities can be directly used in theoretical models to describe the dynamics. Instead, the equivalent of the particle volume fraction is needed where the volume occupied by the particles is used to describe the extent of their interactions. The volume fraction ϕ is determined as c/c^*, where c^* is the overlap mass concentration of particles according to $c^* = M_{total}/\left(4\pi d_{eff}/3R_H^3\right)$ (in weight of polymer per weight of solution), where M_{total} is the total mass of a core-shell particle with $M_{total} = m_c + f M_w/N_A$, where m_c is the mass of the core, f is the number of grafted chains, M_w is the molecular weight of an attached chain, and N_A is the Avogadro number. The c^* represents the average density of the chain (or particle) with radius R_H, and thus, when the total concentration of the system is higher than c^*, the chains (or particles) start to interpenetrate. In monodisperse hard spheres, this would actually take place at $\phi = 0.64$ (which is the random close packing volume fraction). Therefore, we should keep in mind that for HSs $\phi = c/c^* = 0.64$

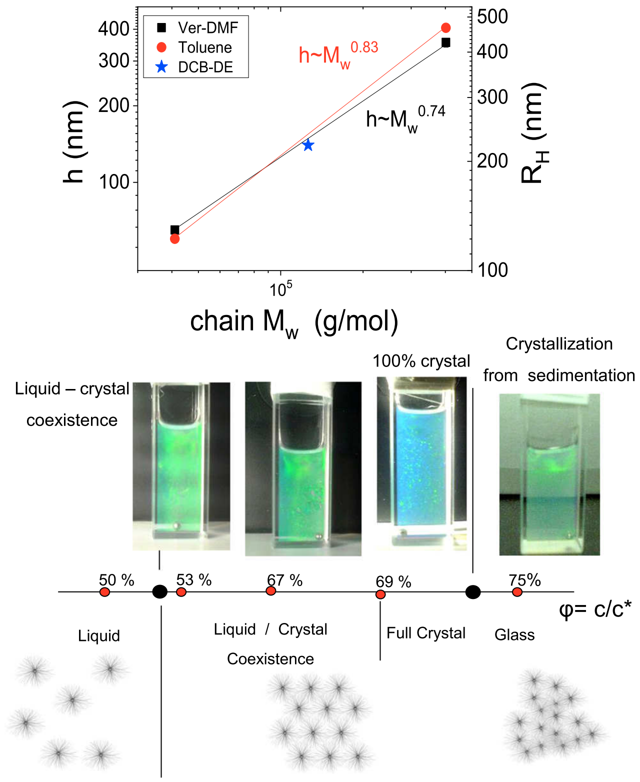

FIG. 2. Top: Molecular weight dependence of the particle shell thickness $h = R_H - R_c$ (left vertical axis) and hydrodynamic radius R_H (right axis) for all considered core-shell systems. Different colors represent different employed solvents. Middle: Picture of *P2_126k* samples at different ϕ where the liquid-crystal coexistence, crystalline phase, and glassy state can be seen. Bottom: Schematic phase diagram for the *P2_126k* particle sample in DCB-DE indicating the succession of different phases.

is where the particles with radius R_H start touching. An alternative common way to effectively determine a volume fraction ϕ in soft particle suspensions is by fitting the measured zero-shear viscosity, η, in the dilute regime with the Batchelor-Einstein prediction for hard spheres, $\eta/\eta_0 \approx 1 + 2.5\phi + 5.9\phi^2$, with η_0 as the solvent viscosity. However, this quadratic order virial expansion expression is for hard spheres with stick hydrodynamic boundary condition only (no-slip spheres). While the quadratic order result can be generalized to soft and permeable particle suspensions, with some numerical effort regarding the quadratic order (Huggins) coefficient, we stick to $\phi = c/c^*$ as a direct estimate of the volume fraction associated with the particle hydrodynamics radius, R_H. We confront then the permeable sphere predictions directly with experimental data as a function of $\phi = c/c^*$. According to our direct observations (Fig. 2) for *P2_126k* particles in DCB-DE, the liquid-crystal coexistence regime extends from about $\phi \sim 0.53$ to ~0.72 where the suspension becomes fully crystalline. Similar phase diagrams were obtained for *P2_41k* and *P2_402k* in veratrole-DMF and toluene. In comparison with colloidal hard spheres (HSs), the liquid-crystal coexistence regime is distinctly broader, while the glass transition volume fraction (of value 0.58 for hard spheres), as estimated by dynamic light scattering and rheological experiments, is shifted to larger values, i.e., $\phi = 0.75$, due to the deformation and possible interpenetration of adjacent polymer shells.

In a study for similar albeit smaller soft particles, Voudouris *et al.*[9] argued that for $R_{DC}/L \approx 1$ core-shell particles behave as hard spheres. In the present work, we take the ratio R_{DC}/R_H as a measure of particle softness since similar particles were dispersed in different solvents and thus the hydrodynamic radius varies both with the grafted polymer molecular weight and the solvent. Table I summarizes the characteristic parameters of the different systems 1–5 (particles/solvent) presently explored, namely, the hydrodynamic radius, R_H; surface grafting density, σ_0; number of grafted chains; particle softness parameter, R_{DC}/R_H; and effective polymer density at the outer blobs. Samples 1–5 are the systems studied in this work, while for comparison we include the corresponding parameters for multiarm star polymers and other soft particles used in the literature (samples 6–9 in the table with corresponding citation numbers). Figure 2 (top) shows the molecular weight dependence of the polymer shell thickness, $h = R_H - R_c$, for the different particles and solvents used. The effect of the solvent is minimal for smaller particles (*P2_41k*) with shorter polymer grafted layers and becomes more pronounced for larger particles (*P2_402k*), as the latter have longer grafted chains that are not stretched in the outer shell and

TABLE I. Characteristic properties of the silica-grafted PMMA core-shell particles studied here (samples 1–5). For comparison regarding the degree of softness, the parameter values of similar systems taken from the literature are added. Samples 6–7: silica particles grafted with a PS shell; Sample 8: silica particles grafted by a PDMS shell, and sample 9: PB star polymers having $f = 128$ arms.

No.	Sample name	R_{SLS} (nm)	R_H (nm)	N_{chains}/nm^2 (σ_0)	N_{chains}/particle (f)	c^* in (g/g)	$\frac{R_{DC}}{R_H}$	σ_{eff} outer blob (nm^{-2})
1	*P2_41k* (Ver-DMF)	119	133	0.55	34 500	0.418	1.00	0.138
2	*P2_41k* (toluene)	119	123	0.55	34 500	0.532	1.08	0.154
3	*P2_126k* (DCB-DE)	194	205	0.65	34 500	0.202	0.62	0.065
4	*P2_402k* (Ver-DMF)	396	420	0.65	34 500	0.077	0.305	0.016
5	*P2_402k* (toluene)	382	470	0.65	34 500	0.067	0.27	0.012
6	SiP-PS short[8]	36	29	0.84	1 056	. . .	0.90	0.098
7	SiP-PS long[8]	70	67	0.50	628	. . .	0.27	0.011
8	SiP-PDMS[3]	180	196	0.008	3 114	. . .	0.17	0.007
9	*Star* 12880[14]	. . .	~60	. . .	128	. . .	0.28	0.003

thus more amenable to size variation due to solvent quality changes. The increase in the polymer shell thickness with polymer chain M_w is following a power law with exponent from 0.74 to 0.83 depending on the solvent.

B. Experimental techniques

To eliminate any residual multiple scattering in concentrated suspensions arising from incomplete refractive index matching between particles and solvent, we have used 3D dynamic light scattering (3D-DLS) to measure both static and dynamic correlation functions. In 3D-DLS,[26–28] two incident beams are used at different scattering planes, with the corresponding scattered beams detected at the same scattering wavevector and then cross-correlated. To achieve this, the initial $(\mathbf{k}_1^i, \mathbf{k}_2^i)$ and final $(\mathbf{k}_1^f, \mathbf{k}_2^f)$ wavevector pairs are rotated by some angle about the common scattering vector $\mathbf{q} = \mathbf{q}_1 = \mathbf{q}_2$ of magnitude q for the two scattering processes 1–1 and 2–2, whereas the two other scattering processes 1–2 and 2–1 detected in this experiment have different scattering vectors. These additional scattering processes will therefore contribute to the background only, which means that the maximum intercept in the 3D-DLS correlation function can reach ideally only 0.25 of the maximum value obtained for autocorrelation at the absence of multiple scattering,[27] as the scattered light from the first (second) beam can fall also into the second (first) detector. Thus, the cross-correlation intensity correlation function is

$$g^{(2)}(q,t) = \frac{\langle I_1^i(0) I_2^i(t)\rangle + \langle I_1^i(0) I_2^{ii}(t)\rangle}{\langle I\rangle^2} + \frac{\langle I_1^{ii}(0) I_2^i(t)\rangle + \langle I_1^{ii}(0) I_2^{ii}(t)\rangle}{\langle I\rangle^2}, \tag{1}$$

where t is the delay time between the correlated scattering intensities, with subindices 1 and 2 labeling the two detectors and the indices i and ii denoting the two different incident beams. Hence, in the 3*D* cross-correlation scheme, the undesired multiple scattering contributions are still detected by the detector [Avalanche Photon Detectors (APDs)], but they produce different scattering vectors $\mathbf{q}_1 \neq \mathbf{q}_2$ and are therefore uncorrelated. In the equation above, only the second term gives correlated contributions to $g^{(2)}(q, \tau)$. Therefore, it yields

$$\begin{aligned} g^{(2)}(q,t) &= \frac{3\langle I_1\rangle\langle I_2\rangle + \langle I_1^i(0), I_2^{ii}(t)\rangle}{\langle I_1^i + I_1^{ii}\rangle\langle I_2^i + I_2^{ii}\rangle} = \frac{3}{4} + \frac{1}{4}\left[1 + \beta_{tot}^2[C(q,t)]\right] \\ &= 1 + \beta_{tot}^2[C(q,t)], \end{aligned} \tag{2}$$

where $C(q, t) = S(q, t)/S(q)$ is the normalized dynamic structure factor (or intermediate scattering function) and $\beta_{tot}^2 = \beta^2 \beta_{OV}^2 \beta_{MS}^2 \beta_T^2$ includes all correction factors reducing the intercept of the correlation function, i.e., β^2 is the coherence area factor, β_{OV}^2 is the two beam scattering volume overlap factor, β_{MS}^2 is the multiple scattering factor, and β_T^2 is the instrumental factor which for 3D-DLS is 0.25.[28,29] Although ideally in the dilute regime we have $\beta_{tot}^2 = 0.25$, in our setup due to the imperfect alignment and beam overlapping, we get a maximum value of $\beta_{tot}^2 = 0.21$. Any further decrease in β_{tot}^2 is due to the multiple scattering factor, β_{MS}^2, that increases with concentration. Therefore, β_{MS}^2 can be calculated as the ratio of the value of the intercept of the correlation function in the concentrated sample to the corresponding dilute sample (where no multiple scattering is present) according to

$$\beta_{MS}^2 = \frac{(g^{(2)}(q,t=0)-1)_{conc}}{(g^{(2)}(q,t=0)-1)_{dil}} = \frac{\beta_{conc}^2}{\beta_{dil}^2}. \tag{3}$$

Here, the superscript "dil" denotes the dilute and "conc" denotes the concentrated suspensions. The single-scattering contribution to the intensity, $I^s(q)$, is then determined as

$$I^s(q) = \beta_{MS} I_{conc}(q). \tag{4}$$

In determining $S(q)$, one needs to account additionally for scattering loss parameters such as the correction factor β_{tot}^2 and the sample transmission. The static structure factor is calculated then from

$$S(q) = \frac{I^s(q) c_{dil} T_{dil}}{I_{dil}(q) c_{conc} T_{conc}}, \tag{5}$$

where c is the particle mass concentration, and T_{conc} and T_{dil}(=1) are the transmissions (ratio of transmitted to incident intensity) for the concentrated and dilute (reference) samples, respectively. Several studies[28,30,31] have demonstrated the applicability of the 3D-DLS approach to successfully probe the dynamics in quite turbid suspensions, for a transmission as low as 4%.

The key quantity determined in DLS as a function of scattering wavenumber q and correlation time t is the dynamic structure factor $S(q, t)$ which reduces to $S(q)$ for $t = 0$. For short times, $S(q, t)$ decays exponentially due to the short-time particle diffusion, according to[18]

$$C(q, t \ll \tau_D) = \frac{S(q, t \ll \tau_D)}{S(q)} = \exp\left[-q^2 D(q)\, t\right], \tag{6}$$

where $\tau_D = R_H^2/D_0$ is a characteristic single-particle diffusion time over the distance set by the hydrodynamic particle radius, with $D_0 = k_B T/(6\pi\eta_0 R_H)$ denoting the single-particle Stokes-Einstein-Sutherland diffusion coefficient. For the considered PMMA-SiP core-shell particles, $\tau_D \sim$ 18–200 ms. The short-time diffusion function $D(q)$ obtained in DLS characterizes the decay of thermal concentration fluctuations of wavelength $2\pi/q$. In the dilute limit where the particles are uncorrelated, $D(q)$ reduces to D_0 where from the latter the (zero-concentration) hydrodynamic radius R_H can be inferred, for known solvent viscosity η_0 at given temperature T.

III. THEORETICAL MODELING

A. Diffusion and hydrodynamic functions

The diffusion function $D(q)$ can be expressed in terms of the ratio[32]

$$D(q) = D_0 \frac{H(q)}{S(q)}, \tag{7}$$

of the positive valued hydrodynamic function $H(q)$ and $S(q)$, times the Stokes-Einstein-Sutherland single-particle diffusion coefficient D_0. The hydrodynamic function plays the role of a generalized short-time sedimentation coefficient in a spatially homogeneous suspension, and it directly reflects the influence of the HIs. At infinite dilution or in the hypothetical absence of HIs, $H(q)$ is identically equal to one. HIs give rise to undulations in $H(q)$ at nonzero particle concentrations. The principal peak value, $H(q_m)$, of $H(q)$ is located at the structural nearest-neighbor wavenumber q_m where also the principal peak of $S(q)$ is observed.

For large wavenumbers $q \gg q_m$, $H(q)$ becomes wavenumber-independent and equal to the normalized short-time self-diffusion coefficient, D_S/D_0, characterizing the initial slope of the particle mean-squared displacement, while $H(0) \approx H(q \ll q_m)$ is equal to the sedimentation coefficient in a homogeneous, monodisperse suspension subjected to a weak and uniform (gravitational) force field. According to Eq. (7), $D(q)$ is determined both by the hydrodynamic factor $H(q)$ and the microstructural factor $1/S(q)$, with the latter being independent of HIs in equilibrium. The diffusion function attains its maximum at $q = 0$, with $D(q = 0) = D_0(H(0)/S(0))$ being distinctly larger than D_0 for higher concentrations. This maximum is due to the collective diffusive (short-time) motion of particles allowing for a fast relaxation of long-wavelength concentration fluctuations. Note that both $H(q)$ and $S(q)$ attain their minimum at zero wavenumber and that $S(0)$ is identical to the osmotic compressibility factor which for concentrated suspensions of repelling particles is distinctly smaller than one. The zero-q diffusion function value, $D(0)$, is commonly referred to as collective diffusion coefficient since in the fluid phase it agrees practically with the macroscopic collective or gradient diffusion coefficient D_C. The latter appears in the Fick constitutive law which linearly relates the macroscopic diffusion current and concentration gradient. The principal minimum of $D(q)$ is located at q_m where $S(q)$ and $H(q)$ have their respective principal maximum, with $S(q_m)$ being typically distinctly larger than $H(q_m)$.

The slowing down of concentration fluctuation relaxations on length scale $2\pi/q_m$ is quantified by the cage diffusion coefficient $D(q_m)$ whose value decreases with increasing concentration and increasing strength of interparticle repulsion. For large wavenumbers $q \gg q_m$ where spatial correlations over short distances are probed, $D(q)$ becomes equal to the short-time self-diffusion coefficient D_S. Due to HIs, D_S is smaller than D_0 both when repulsive and attractive direct (i.e., nonhydrodynamic) interactions are operative.

In theory and simulations, $H(q)$ is commonly calculated from the equilibrium ensemble average expression[32]

$$H(q) = \left\langle \frac{1}{N\mu_0} \sum_{l,j=1}^{N} \hat{\mathbf{q}} \cdot \boldsymbol{\mu}_{lj}(X) \cdot \hat{\mathbf{q}} \exp\{i\mathbf{q} \cdot (\mathbf{r}_l - \mathbf{r}_j)\} \right\rangle, \tag{8}$$

for a system of $N \gg 1$ interacting spherical particles at center position configuration $X = \{\mathbf{r}_1, \ldots, \mathbf{r}_N\}$. Here, $\boldsymbol{\mu}_{lj}(X)$ is the hydrodynamic mobility tensor linearly relating the hydrodynamic drag force on particle j to the resulting velocity change of particle l, and $\mu_0 = D_0/(k_B T)$ is the single-sphere mobility. At high dilution, $\boldsymbol{\mu}_{lj}(X)$ reduces to $\mu_0 \delta_{lj} \mathbf{1}$ with unit matrix $\mathbf{1}$ and Kronecker delta δ_{lj}, and $H(q)$ becomes then a constant equal to one. We emphasize that the hydrodynamic function is determined both by HIs and direct (i.e., nonhydrodynamic) interactions. Only the latter determine the equilibrium configurational average in Eq. (8) denoted by $\langle \cdots \rangle$.

B. Hydrodynamic radius and spherical annulus models

Both $\boldsymbol{\mu}_{lj}(X)$ and μ_0 depend on the internal hydrodynamic particle structure. In the hydrodynamic radius model (HRM), a spherical particle of arbitrary internal structure is described hydrodynamically as a no-slip sphere of reduced radius R_H, for unchanged direct interaction potential.[10,33] This implies, in particular, an unchanged (effective) excluded volume radius $R_{\mathit{eff}} > R_H$. Despite its simplicity, as is shown in Ref. 34, the HRM is universally applicable since correction terms to the HRM based dynamic properties are quite small, i.e., of quadratic order in the reduced slip length $\overline{\gamma} = 1 - \gamma$, where $\gamma = R_H/R_{\mathit{eff}}$. The reduced hydrodynamic radius, γ, in the HRM can be related to particle specific properties such as the (mean) Darcy permeability k characterizing the solvent permeability of a particle. The square root of k is identified as the hydrodynamic penetration length. For uniformly permeated particles having constant $x = R_{\mathit{eff}}/\sqrt{k}$, the relation between γ and x is[35]

$$\gamma(x) = \frac{R_H(x)}{R_{\mathrm{eff}}} = \frac{2x^2[x - \tanh(x)]}{2x^3 + 3[x - \tanh(x)]} \approx 1 - \frac{1}{x} + \mathcal{O}\left(\frac{1}{x^2}\right). \tag{9}$$

Here, $\gamma(x) = D_0(x = \infty)/D_0(x)$ with $D_0(x = \infty) = k_B T/(6\pi\eta_0 R_{\mathit{eff}})$ is the single-particle translational diffusion coefficient of a nonpermeable rigid sphere having zero solvent slip at its surface. If dynamic properties different from $D(q)$ are considered such as the suspension viscosity, corresponding relations between γ and x should be used which differ from the present one, however, only by small corrections of $\mathcal{O}(1/x^2)$.[33] Regarding the here considered core-shell particles with a permeable polymer brush of radially varying density, and a nonpermeable (or less permeable) core, x can be regarded as an average inverse penetration length. When the shell thickness is at least five times $\sqrt{k}$, the core is not sensed any more hydrodynamically by the weakly penetrating solvent.[36]

Provided the (core-shell) particles can be described, regarding their direct interactions, as (effective) hard spheres of volume fraction $\phi_{\mathit{eff}} = (4\pi/3)nR_{\mathit{eff}}^3$ with n denoting the number concentration of particles, the HRM reduces to the spherical annulus model which is fully characterized by ϕ_{eff} and $\gamma = R_H/R_{\mathit{eff}}$. No-slip colloidal hard spheres are recovered in the limit $\gamma \to 1$. The mathematical limit $\gamma = 0$ describes hypothetical particles that interact directly as hard spheres but hydrodynamically as point particles without hydrodynamic back reflections. For the spherical annulus model, simple analytic expressions for the normalized short-time self-diffusion coefficient $D_S(\phi_{\mathit{eff}}, \gamma)/D_0(\gamma)$ and the sedimentation coefficient $H(q = 0; \phi_{\mathit{eff}}, \gamma)$ have been presented in Ref. 10. These expressions agree well with the high-precision hydrodynamic force multipole simulation (HYDROMULTIPOLE) results obtained by Abade *et al.*[36,37] for the γ and ϕ_{eff} values considered in the simulations ($\phi_{\mathit{eff}} \leq 0.45$) and with the Stokesian dynamics simulation results obtained by Banchio and Brady[17] and Banchio and Nägele[20] for no-slip colloidal hard spheres ($\gamma = 1$) in the fluid phase ($\phi_{\mathit{eff}} \leq 0.5$). The explicit form of these expressions is[10]

$$\frac{D_S(\phi_{\mathit{eff}}, \gamma)}{D_0(\gamma)} = 1 + \lambda_t(\gamma)\,\phi_{\mathit{eff}}\left(1 + 0.12\phi_{\mathit{eff}} - 0.70\phi_{\mathit{eff}}^2\right) \tag{10}$$

and

$$H(0;\phi_{eff},\gamma) = 1 + \lambda_K(\gamma)\phi_{eff}\Big[1 - 3.348(\gamma\phi_{eff}) + 7.426(\gamma\phi_{eff})^2 - 10.034(\gamma\phi_{eff})^3 + 5.882(\gamma\phi_{eff})^4\Big], \tag{11}$$

with approximate first-order virial coefficients

$$\lambda_t(\gamma) = -1.8315 + 7.820\overline{\gamma} - 14.231\overline{\gamma}^2 + 14.908\overline{\gamma}^3 - 9.383\overline{\gamma}^4 + 2.717\overline{\gamma}^5, \tag{12}$$

$$\lambda_K(\gamma) = -6.5464 + 8.592\overline{\gamma} - 3.901\overline{\gamma}^2 + 2.011\overline{\gamma}^3 - 0.142\overline{\gamma}^4, \tag{13}$$

where $D_0(\gamma) = D_0(1)/\gamma$ and $\overline{\gamma} = 1 - \gamma$. In the zero-annulus limit $\gamma = 1$, the numerically precise first-order virial coefficients $\lambda_t(1) = -1.8315$ and $\lambda_K(1) = -6.5464$ of no-slip hard spheres are recovered. The expressions for $D_S(\phi_{eff}, \gamma)/D_0(\gamma)$ and $H(0; \phi_{eff}, \gamma)$ given above are valid for volume fractions up to the hard-sphere freezing transition value $\phi_{eff}^{(f)} = 0.494$. The self-diffusion coefficient expression is valid generally for $0 \le \gamma \le 1$, while the zero-wavenumber hydrodynamic function expression is of good accuracy in the restricted range $0.8 < \gamma \le 1$ only which still includes most experimental cases. In the limit $\gamma \to 0$, it holds exactly that $H(q; \phi_{eff}, \gamma = 0) = 1$ and consequently that $\lambda_t(0) = 0$ and $\lambda_K(0) = 0$.

In Refs. 10 and 37, it is shown that the ratio $H_d(q; \phi_{eff}, \gamma)/H_d(0; \phi_{eff}, \gamma)$ is, for $qR_{eff} \ge 2$, practically independent of γ, for particles having hard-sphere or soft (Hertzian potential) direct interactions. Here, $H_d(q) = H(q) - D_S/D_0$ is the wavenumber-dependent, so-called direct part of the hydrodynamic function. This allows for approximating the hydrodynamic function for $\gamma < 1$ and $qR_{eff} \ge 2$ by[10,37]

$$H(q;\gamma) \approx \left[\frac{\frac{D_S(\gamma)}{D_0(\gamma)} - H(0;\gamma)}{\frac{D_S(1)}{D_0(1)} - H(0;1)}\right]\left[H(q;1) - \frac{D_S(1)}{D_0(1)}\right] + \frac{D_S(\gamma)}{D_0(\gamma)}, \tag{14}$$

i.e., in terms of the hydrodynamic function, $H(q; 1)$ of no-slip hard spheres where $\gamma = 1$. For $H(0; \gamma)$ and $D_S(\gamma)$, the expressions in Eqs. (11) and (10) are used as input, respectively. For conciseness, in Eq. (14), the ϕ_{eff} dependence of H and D_S is not displayed. Equation (14) specializes to $D_S(\phi_{eff}, \gamma)/D_0(\gamma)$ for $q \to \infty$ and to $H(0; \phi_{eff}, \gamma)$ for $q \to 0$.

While no simple analytic formula is known describing the general q dependence of the no-slip hard-sphere $H(q; \phi_{eff}, 1)$, its principal peak height value is given to excellent accuracy, and for all $\phi_{eff} \le \phi_{eff}^{(f)}$, by the linear form[20]

$$H(q_m;\phi_{eff};1) = 1 - \phi_{eff}/\phi_{eff}^{cp} = 1 - 1.35\,\phi_{eff}. \tag{15}$$

which after insertion into Eq. (14) results in an analytic expression for the hydrodynamic function peak height, applicable to good accuracy for $0.8 < \gamma < 1$ and reducing to Eq. (15) for $\gamma = 1$. Here, $\phi_{eff}^{cp} = \pi/(3\sqrt{2}) \approx 0.74$ is the largest possible volume fraction of monodisperse rigid spheres, realized in closest packed (cp) fcc and hcp crystalline structures.

An analytic expression for the cage diffusion coefficient, $D(q_m; \phi_{eff}, \gamma)$, follows from dividing $H(q_m; \phi_{eff}, \gamma)$ according to Eqs. (14) and (15), by the hard-sphere structure factor peak height expression,[38]

$$S(q_m;\phi_{eff}) = 1 + 0.644\,\phi_{eff}\,\frac{1 - \phi_{eff}/2}{(1 - \phi_{eff})^3}, \tag{16}$$

which holds accurately in the fluid phase up to the freezing transition concentration where $S(q_m; \phi_{eff}^{(f)}) = 2.85$ in accord with the Hansen-Verlet freezing criterion for hard spheres.[39,40] Consequently, it is $D(q_m; \phi_{eff}^{(f)}, 1)/D_0(1) \approx 0.12$ at freezing. With decreasing γ departing from the no-slip value one, $D(q_m; \phi_{eff}^{(f)}, \gamma)/D_0(\gamma)$ increases initially monotonically, passes then through a maximum at about $\gamma \approx 0.5$, and decreases subsequently toward $1/S(q_m; \phi_{eff}^{(f)}) = 0.35$ reached for $\gamma = 0$.

The collective diffusion coefficient follows analytically from dividing $H(0; \phi_{eff}, \gamma)$ according to Eq. (11) by the Carnahan-Starling hard-sphere osmotic compressibility factor expression[10]

$$S(0;\phi_{eff}) = \frac{(1 - \phi_{eff})}{(1 + 2\phi_{eff})^2 + \phi_{eff}^3(\phi_{eff} - 4)}, \tag{17}$$

valid to high accuracy in the fluid phase up to $\phi_{eff}^{(f)}$, and in the metastable isotropic (disordered) state even up to $\phi_{eff} = 0.57$.

At the RCP volume fraction $\phi_{eff}^{(rcp)} \approx 0.64$ of genuinely monodisperse hard spheres constituting the concentration maximum of the metastable isotropic phase, the osmotic compressibility factor $S(0)$ becomes zero, whereas $S(q_m) \approx 4$, as shown by elaborate computer simulation results for $S(q)$.[41] When the hard spheres are strictly jammed at random close packing so that they cannot move relative to each other, one expects $D_S = 0$ and $H(q_m) = 0$, and consequently a vanishing cage diffusion coefficient $D(q_m) = 0$. In experimental RCP suspensions, residual particle polydispersity and softness, and the presence of a small fraction of tiny crystallites gives rise to values of $S(0)$ and $D(q_m)$ at $\phi_{eff}^{(rcp)}$ which are not strictly zero.[42] Note further that both the high-frequency (short-time) and zero-frequency (long-time) suspension viscosities are diverging at random close packing.

To calculate $H(q; \phi_{eff}, \gamma)$ for $qR_{eff} \ge 2$, Eq. (14) is used in combination with the Beenakker-Mazur (BM) 2nd-order $\delta\gamma$ mean-field method[43] by which the *distinct* hydrodynamic function input, $H_d(q; \phi_{eff}, 1)$, of no-slip hard spheres is calculated.[10] At $\gamma = 1$ and $q = q_m$, the so-obtained hydrodynamic function peak height follows decently well the accurate linear form $1-1.35\phi_{eff}$ up to $\phi_{eff} \approx 0.4$. With further enlarged ϕ_{eff}, the linear form is somewhat overestimated but to a lesser extent than when the BM prediction for $H(q_m; \phi_{eff}, 1)$ is used.

While not needed for the present short-time diffusion analysis of core-shell colloids, we note that for the spherical annulus model, analytic expressions are available also for the long-time self-diffusion coefficient $D_L(\phi_{eff}, \gamma)$, and the high- and zero-frequency viscosities $\eta_\infty(\phi_{eff}, \gamma)$ and $\eta(\phi_{eff}, \gamma)$, respectively.[10] While the overall influence of solvent permeability is well treated within the analytical spherical annulus model, treating core-shell particles statically (i.e., nonhydrodynamically) as effective hard spheres is an oversimplification for extended soft polymer shells. However, the simple model can still be useful for exploring general trends in these systems, as is done in Sec. IV.

IV. RESULTS AND DISCUSSION

A. Dilute regime: Form factor and interactions

Static light scattering intensity in the dilute regime is used to determine the particle form factor, $F(q) = I_{dil}(q)/I_{dil}(q = 0)$, which describes intraparticle interference effects in the scattering intensity and provides information on the size, shape, and internal structure of the scatterers. For all systems considered, $F(q)$ is strongly q-dependent, and it can be fitted using a core-shell particle model with homogeneous core and in general an inhomogeneous shell. Figure 3 shows the experimental form factor (symbols) for different systems corresponding to particles with different shells and therefore varying softness dictated also by the total particle size and/or the solvent quality. The data were fitted with an adaptation from "SCATTER" software[44] (ESRF).

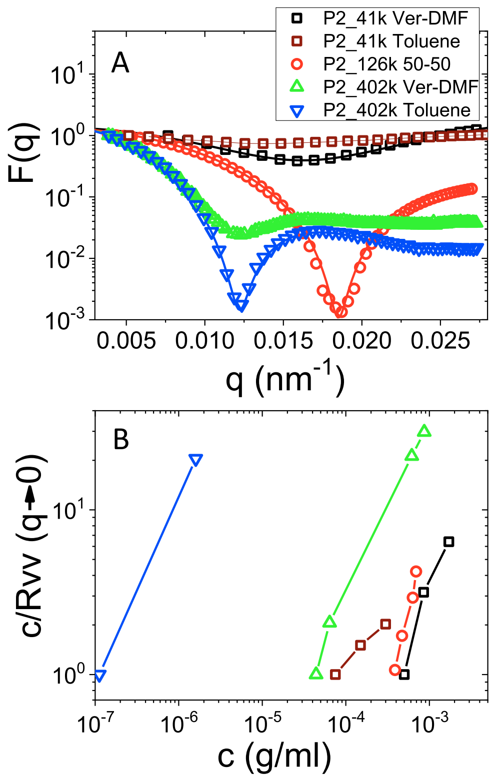

FIG. 3. (a) Particle form factor as a function of the scattering wavenumber q. Open symbols are experimental (SLS) data, and solid lines are fits using the core-shell model. From the fits, the core-shell model radii values 130 nm (for *P2_41k* Ver-DMF), 173 nm (for *P2_41k* toluene), 194 nm (for *P2_126k*), 396 nm (for *P2_402k* Ver-DMF), and 382 nm (for *P2_402k* toluene) are deduced. (b) SLS experimental data for c/R_{vv} (in g/cm^2), for all systems 1–5. In all cases, $A_2 > 0$ indicative of repulsive particle interactions.

The form factor of the smaller and less soft particles *P2_41k* exhibits a minimum at $q = 0.016$ nm^{-1} for both solvents, corresponding to an overall effective HS radius of 280 nm. In toluene, this minimum is less pronounced than that for the veratrole-DMF solvent mixture. The core-shell model fit gives a total radius of 130 nm in the veratrole-DMF and 173 nm in toluene. For the intermediately sized (and softness) particles, *P2_126k*, $F(q)$ exhibits a minimum at $q = 0.0185$ nm^{-1} (red circles) corresponding to an effective HS radius of 242 nm, while the core-shell model yields a total radius of 194 nm. The largest particle system *P2_402k*) yields for both solvents (veratrole-DMF and toluene) a form factor minimum at a similar wavenumber $q = 0.012$ nm^{-1}. However, the minimum is deeper in toluene, in contrast to what is observed for the smaller, *P2_41k*, particles. The total radii in the two solvents were found to be 420 nm and 470 nm in veratrole-DMF and toluene, respectively.

In addition to the total particle size, static light scattering data measured at different concentrations in the dilute regime allow for an estimation of the second virial coefficient, A_2, thus providing information about interparticle interactions, with positive values of A_2 indicating repulsive interactions and negative values of A_2 indicating attractive interactions. The coefficient A_2 (in units of mol × ml/g^2) can be determined from $\frac{Kc}{R_{vv}} = \frac{1}{M_w} + 2A_2c$, where M_w is the molecular weight (in g/mol) of the scatterers, c is their mass concentration (in g/ml), R_{vv} is the excess Rayleigh ratio (yielding the absolute scattering intensity), and $K = \frac{4\pi^2 v_0^2}{N_A\lambda^4}(\frac{dv}{dc})^2$ is a constant related to the optical properties of the sample (with N_A as the Avogadro number and dv/dc as the refractive index increment of the specific particle-solvent system[45]). All considered systems (particle/solvent combinations) yield positive second virial coefficients and therefore repulsive interactions. Table II lists the parameters used in fitting the form factor. For the smaller particles *P2_41k*, R_{DC} coincides with the total radius of the particle, i.e., the grafted chains are fully stretched due to their excluded volumes. Thus, we expect here a behavior close to that of hard spheres. For the two other particle systems *P2_126k* and *402k*, the size of the grafted polymer shell, $h = R_H - R_c$, is significantly larger than the core size [as seen in Fig. 2 (top)]; hence, a behavior departing from that of hard spheres should be expected. In addition, we used DLS to determine the hydrodynamic radius, R_H, in the dilute regime (see Table II) based on the Stokes-Einstein-Sutherland diffusion coefficient expression. The R_H values obtained are consistently but only slightly larger than the total particle radii deduced from static light scattering.

B. Concentrated suspensions

1. Static properties

Figure 4 depicts static scattering intensity data, normalized by particle mass concentration c, as a function of qR_H for different volume fractions, ϕ, indicated in the figure, and for the four considered particles/solvent systems. In all cases, the intensity curves have qualitatively the behavior observed for colloidal suspensions in the liquid regime, with a refining peak in the scattering intensity as the concentration is increased. Moreover, the peak position, q_m, moves to higher q_mR_H values and sharpens owing to the increasing probability

TABLE II. Parameters used in fitting the experimental form factor by the core-shell model, and particle characteristic values deduced from static and dynamic light scattering data, with ν_c as the refractive index of the core, ν_0 as refractive index of the solvent, and σ_c as the fitting parameter for the polydispersity of core. Note that the polydispersity index deduced here from the form factor fits are similar but not identical with the nominal one of 0.10, deduced by TEM.

Sample name	$P2\_41k$ (Ver-DMF)	$P2\_41k$ (toluene)	$P2\_126k$ (DCB-DE)	$P2\_402k$ (Ver-DMF)	$P2\_402k$ (toluene)
M_w (kg/mol)	41	41	126	402	402
ν_c	1.479	1.479	1.479	1.479	1.479
ν_0	1.489	1.496	1.489	1.489	1.496
R_c (nm)	65	65	65	65	65
σ_c	0.05	0.12	0.10	0.05	0.05
R_{SLS} (nm)	119	119	194	396	382
R_H (nm)	133	123	205	420	470

of finding particle pairs at the specific distance $r \approx 2\pi/q_m$. At low q, the (normalized) intensity decreases with increasing volume fraction, as one expects from a decreasing osmotic compressibility suppressing large-wavelength concentration fluctuations.

With increasing particle size and hence increasing softness, larger values of qR_H are reached. For the $P2\_402k$ particles (both suspended in toluene and veratrole-DMF), the large qR_H regime is reached where the scattered normalized intensity is nearly volume fraction independent [see Fig. 4(c)]. For the intermediately size, $P2\_126k$, particles, however, the normalized intensity data show an unexpected decrease with increasing ϕ in the assessed qR_H range. For the smallest considered particle system $P2\_41k$, the peak value of the normalized intensity is nearly volume fraction independent, but large qR_H values are not reached in this case. This response of the scattering intensity from the two smaller particle systems indicates that a form factor changes with concentration, precluding the proper determination of the static structure factor at high concentrations. In particular, the first minimum of the scattering intensity, and thus of $S(q)$ at $qR_H \sim 5$, is affected by concentration dependent changes in the minimum of $F(q)$ at $q \sim 5.04$.

The structure factor, $S(q)$, can be determined using Eq. (5), assuming that the form factor does not change at higher concentrations. The so-deduced structure factor for the $P2\_402k$ particles in veratrole-DMF based on Eq. (5) is displayed in Fig. 5. The observation that $S(q)$ at large q values approaches 1 indicates that the assumptions underlying Eq. (5) are fulfilled in this case. By contrast, for all the other samples, it is evident that $S(q)$ cannot be successfully deduced from the scattering data in conjunction with Eq. (5) since at the large-qR_H limit we do not acquire $S(q) = 1$ independent of the volume fraction. This is demonstrated in the supplementary material. The failure to deduce a proper $S(q)$ using Eq. (5) suggests that the shape of the two smaller particle systems, and hence their form factors, changes with increasing concentration, possibly due to the grafted polymer chain interpenetration and retraction associated with changes in the solvent quality at large concentrations. The oscillations in $S(q)$ seen in Fig. 5 at larger qR_H indicate liquidlike order in the volume fraction range measured here. The first minimum of the deduced $S(q)$ at $qR_H \sim 5$ to the right of the principal peak is affected by the low scattering intensity due to the minimum of the form factor in this wavenumber region that introduces a significant error. A similar shape of $S(q)$ as in Fig. 5 was reported by Laurati *et al.*[46] for starlike micelles at high volume fractions, where it was attributed to a partial crystallization of the sample, as verified by additional small angle neutron scattering (SANS) experiments. For our core-shell suspension, (partial) crystallization is ruled out as a cause for the shape of $S(q)$ as its minimum persists even to low volume fractions with its width increasing as the volume fraction is decreased. Note that crystallization is indeed observed in all systems at higher volume fractions, with a coexistence regime as mentioned above (Sec. II A).

The osmotic compressibility factor, $1/S(q \to 0)$, of the considered core-shell systems strongly decreases with increasing volume fraction. Interestingly, the principal peak height, $S(q_m)$, quantifying the degree of next-neighbor ordering, shows a nonmonotonic behavior with respect to ϕ. At the largest volume fractions close to the liquid-crystal coexistence, the peak is located at $q_m R_H \sim 2.8$ corresponding to significantly larger next-neighbor distance $\sim 2\pi/q_m$ than that in a hard-sphere suspension at liquid-crystal freezing for which $qR_H \sim 3.5$ (at $\phi < 0.494$). Similar longer-range interactions were also observed in other soft colloids and spherical micelles such as PEO-PEP starlike micelles at $\phi = 1$ reported by Laurati *et al.*[46] [see Fig. 5(b)].

The long-range repulsion can be attributed to the presence of dangling chain ends in the outer blobs of the polymer-grafted particles which do not contribute significantly to the scattering intensity. Consequently, R_H and R_{tot} are somewhat underestimated, while a weak longer-range repulsion for pair distances larger than the measured values for $2R_H$ and $2R_{tot}$ is induced. It should be noted that no additional long-range electrostatic interactions are expected to occur since the particles are not charged. Moreover, only weak residual van der Waals attractions are expected, owing to the refractive index matching of the polymer shells and the larger mutual distance of the cores of neighboring particles enforced by the steric hindrance provided by the polymeric shells.

The volume fraction dependence of the wavenumber position, q_m, of the principal peak of $S(q)$ should be practically equal, for monodisperse suspensions, with the peak position of the minimum of $D(q)$. This wavenumber relates to the (mean) nearest-neighbor distance $\sim 2\pi/q_m$ dependent on the interaction range and strength,

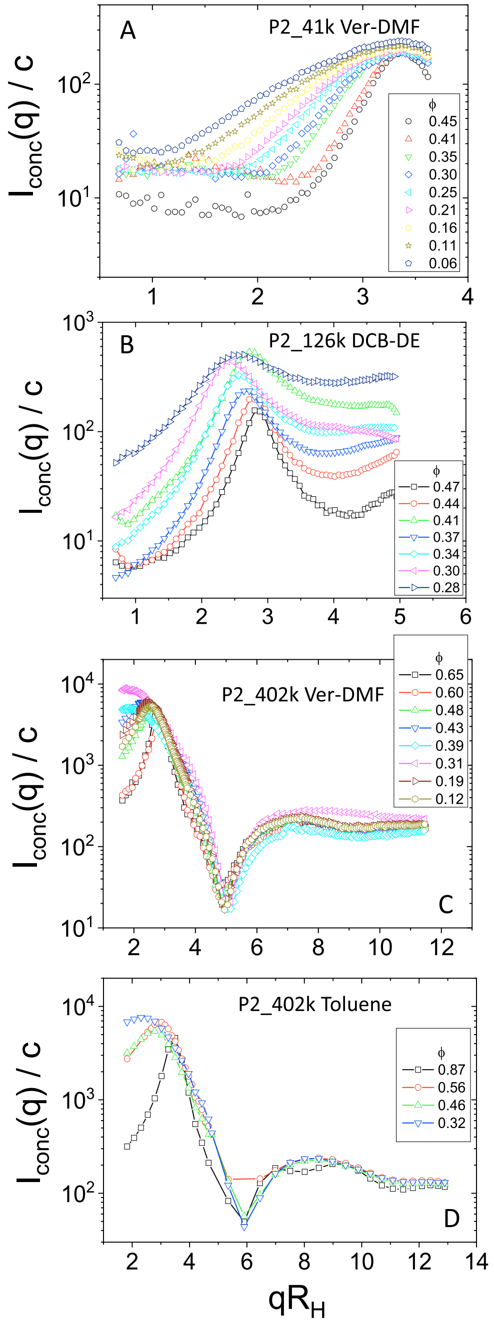

FIG. 4. Static light scattering intensity, $I_{conc}(q)$, divided by the particle mass concentration, c (in gram of particles per gram of solution), as a function of qR_H for all systems studied: (a) *P2_126k* in DCB-DE, (b) *P2_402k* in veratrole-DMF (c), and (d) *P2_402k* in toluene, for several volume fractions, ϕ as indicated in the caption.

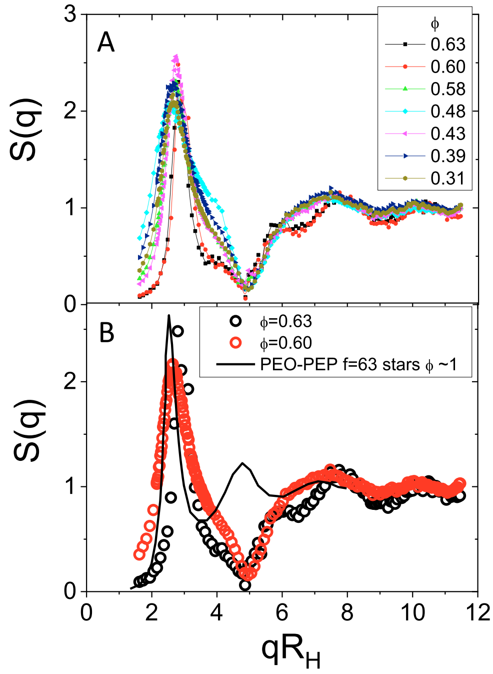

FIG. 5. (a) Experimental (SLS) static structure factor, $S(q)$, determined using Eq. (5), as a function of qR_H for *P2_402k* particles in veratrole-DMF, for various volume fractions as indicated. (b) $S(q)$ of the *P2_402k* system for two different concentrations and compared with the static structure factor of starlike PEO-PEP micelles with f = 63 arms at a similar concentration (solid line) as taken from the work of Laurati *et al.*[46]

and the particle concentration. Results for $q_m R_H$ are presented in Fig. 6 as a function of the volume fraction. It is insightful to compare the q_m for the core-shell particle systems with the corresponding finding for suspensions of hard spheres and for low-salinity suspensions of charge-stabilized spherical spheres. In Fig. 6, the q_m values for colloidal hard spheres (black solid line)are calculated using the Percus-Yevick (PY) approximation, while for charged particles under low salinity conditions with long-range

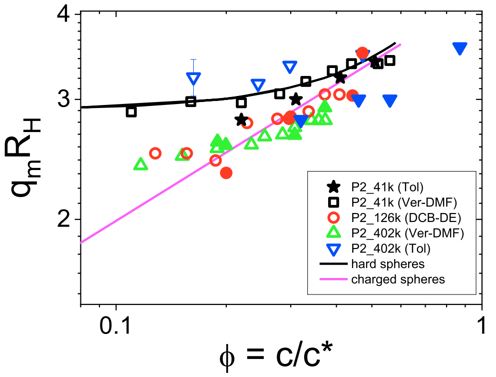

FIG. 6. Wavenumber position q_m of the principal peak of $S(q)$ (open symbols) in units of R_H and as a function of volume fraction ϕ for all considered systems. For comparison, the hard-sphere q_m predicted by the Percus-Yevick (PY) scheme for the fluid concentration regime is included (black solid curve) together with the corresponding result $q_m \propto \phi^{1/3}$ for the peak position of charge-stabilized colloidal spheres under low ionic strength condition (magenta solid line). Further shown (with the corresponding filled symbols) is the wavenumber position of the minimum of $D(q)$ for all systems as taken from Fig. 9.

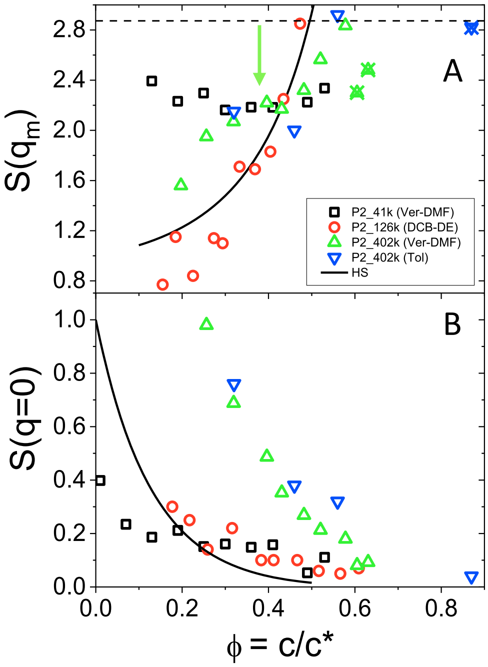

FIG. 7. (a) Structure factor principal peak height, $S(q_m)$, as a function of volume fraction ϕ for all considered core-shell systems as indicated. The solid black curve is the hard-sphere peak height according to Eq. (16), and the horizontal dashed line indicates the Hansen-Verlet peak value 2.85 hallmarking the fluid-crystal freezing transition of hard-sphere-like systems.[39] (b) Zero-q estimated values for the osmotic compressibility factor $S(0)$ as a function of volume fraction, for the indicated core-shell systems. The solid black line is the hard-sphere Carnahan-Starling result in Eq. (17). The depicted data (open symbols) are actually taken for the lowest attained q values.

electric repulsion the empirical formula $q_m R_H \approx 1.1 \times (2\pi R_H) n^{1/3} = 1.1 \times (6\phi\pi^2)^{1/3}$ is used, where n is the particle number density.[8] The particles $P2\_41k$ with the shortest grafted polymer chains (open black squares) have a similar volume fraction dependence of q_m with that of hard spheres (solid black line). For the intermediate sized polymer grafted particles, $P2\_126k$ (red open circles), q_m follows a similar trend as that of hard spheres but with lower values, in particular, at smaller ϕ, implying liquidlike behavior for larger interparticle distances. The maximal deviation from the corresponding hard-sphere q_m is 18%, observed for the lowest considered volume fraction. This deviation can be attributed again to the presence of dangling ends in the outer polymer blob region discussed earlier. Experimental data for q_m of the largest considered core-shell particles $P2\_402k$ bear similarities with that for $P2\_126k$, with the values for q_m being smaller when veratrole-DMF is used as the solvent instead of toluene. Note that the use of an increased effective particle radius size accounting for dangling ends not detected in static or dynamic light scattering would not only enlarge the depicted $q_m R_H$ values but would also affect the abscissa scale in the figure since the true volume fraction is then larger. However, different from hard spheres, soft particles can interpenetrate, deform, and may eventually even shrink at large concentrations.

Figure 7(a) shows the static structure factor principal peak height, $S(q_m)$, for the considered core-shell particle systems as a function of ϕ. The peak height (and its sharpness) is a measure of how strongly the nearest-neighbor particle cage is developed. For hard spheres, $S(q_m)$ increases monotonically in the fluid regime according to Eq. (16), reaching the Hansen-Verlet hard-sphere freezing criterion value 2.85 at the fluid-solid freezing transition volume fraction $\phi^{(f)} = 0.494$.[39] As pointed out earlier, the determination of $S(q_m)$ in most of our samples is affected by the changes in $F(q)$ at large concentrations, causing uncertainties in the extraction of $S(q)$ based on Eq. (5). Nevertheless, it is worth noting that for the smaller and least soft particles $P2\_41k$, the so-determined $S(q_m)$ is nearly volume fraction independent [see Fig. 7(a)]. This hints toward artificially introduced cancellations for increasing concentration caused by particle shrinkage. For the intermediately large particles $P2\_126k$, the peak height $S(q_m)$ increases monotonically with increasing ϕ akin to hard spheres, reaching the Verlet-Hansen value of 2.85 at $\phi \sim 0.45$. Note also that in this system crystal formation is observed around $\phi \sim 0.49$–0.51.

For the larger and softer particles $P2\_402k$ in the veratrole-DMF solvent mixture, $S(q_m)$ increases first with increasing ϕ toward an intermediate plateau region around $\phi \sim 0.3$, rising again subsequently with the Hansen-Verlet hard-sphere freezing value 2.85 reached at $\phi \sim 0.6$ where crystallization of the core-shell particles is visually detected by Bragg scattering. As expected, due to the softness of the particles, crystallization occurs at a higher volume fraction than that for hard spheres (see Fig. 2), for all considered core-shell systems since these are all quite monodisperse. Beyond this freezing volume fraction, the value of $S(q_m)$ decreases for ϕ values extending up to 0.64. This peak height decrease with increasing volume fraction, ϕ, might be due to entering into a crystal-liquid concentration coexistence region where measurements of $S(q)$ are prone to larger errors since a single speckle measurement does not provide the proper ensemble-averaged intensity from different crystalline/liquid regions in the sample. Proper measurement of $S(q)$ in the semicrystalline state requires additional spatial averaging of different parts of the sample, similar to powder crystallography.[18] The structure factor peak height of $P2\_402k$ in toluene exhibits likewise a nonmonotonic volume fraction dependence.

A thermodynamic property monitored is the value of the structure factor at low q which equals to the osmotic compressibility factor given by the ratio of the suspension osmotic compressibility and the corresponding ideal gas compressibility for the same concentration and temperature. Figure 7(b) depicts the deduced low-q structure factor values of the core-shell systems as a function of ϕ. Interestingly, the particles with the shortest grafted polymer chains, $P2\_41k$ and $P2\_126k$, follow roughly the hard-sphere theoretical prediction (solid curve) with the latter being also in good agreement with the experimental zero-q extrapolated measurements for colloidal hard spheres by Segre *et al.*[47] The measured compressibility factor for the largest considered particles, $P2\_402k$, is practically the same in both solvents and distinctly exceeds the hard-sphere values. This is a clear indication of the softness of the outer polymer layer in these systems. We point out that the compressibility factor is estimated by the $S(q)$ value at the lowest attained wavenumber (i.e., at $qR_H \sim 1.5$), rather than by a zero-q extrapolation which would introduce large errors.

2. Dynamic properties

We proceed by discussing short-time diffusion properties of our core-shell systems for different volume fractions, measured using the 3D-DLS setup described in Subsection II B. As noted earlier, the dynamics is not affected by possible concentration-dependent changes in the form factor or in the scattering conditions. The experimental data are interpreted theoretically using for simplicity the spherical annulus version of the HRM described in Subsection III B. The virtue of the spherical annulus model in addition to its conceptual simplicity is that accurate analytic expressions are available for the diffusion (and linear viscoelastic) properties given in Subsection III B. Since the volume fraction of particles ϕ is identified using R_H (from dynamic light scattering) by $(4\pi/3)nR_H^3 = c/c^*$, the effective hard-core radius R_{eff} can be determined via $\gamma = R_H/R_{eff}$, fitting the experimental diffusion data by $D(\gamma)$ in a self-consistent way. The latter requires that every set of experimental $D(\gamma)$ data plotted vs an effective volume fraction, $\phi_{eff} = \phi/\gamma^3$, is represented well by $D(\gamma)$ according to the spherical annulus model.

The normalized measured dynamic structure factor, $C(q, t) = S(q, t)/S(q)$, quantifies correlated relaxations of thermally induced concentrated fluctuation contributions of wavelength $2\pi/q$, associated with self-diffusion for $q \gg q_m$, nearest-neighbor cage relaxation for $q \approx q_m$, and large-wavelength cooperative diffusion for $q \ll q_m$. Figure 8(a) shows the temporal decay of the 3D-DLS $C(q, t)$ for a concentrated suspension at $\phi = 0.47$, at various scattering wavenumbers as indicated (with $q_m = 0.0147$ nm^{-1}). As expected in the fluid phase, the relaxation of $C(q, t)$, toward zero at long-times, is slowing down with increasing volume fraction [Fig. 8(b)]. Consistent with Eqs. (6) and (7) describing the exponential short-time decay (see the insets in Fig. 8), $C(q, t)$ decays most slowly at the wavenumber q_m associated with the extent of the nearest-neighbor cage. This nonmonotonic dependence of the relaxation time with q is depicted with arrows in the inset, where the initial decay of $C(q, t)$ is represented in a log-linear plot. It is worth noting that the shape of $C(q, t)$ remains for the core-shell system largely single exponential. Even as the liquid-crystal coexistence is approached, there is no indication of a clearly distinguishable slower long-time mode related to out-of-cage diffusion, in contrast to hard-sphere and charge-stabilized particle suspensions when a freezing[21] or glass transition point is approached with increasing concentration.

In the dilute regime where particles are practically uncorrelated, the short-time diffusion function, $D(q) \approx D_0$, deduced from $C(q, t)$ is wavenumber independent, and of value equal to the single-particle diffusion coefficient D_0 [see Eq. (7)]. By contrast, in the concentrated regime, $D(q)$ behaves strongly nonmonotonic, with the most pronounced diffusional slowing down reflected by its minimal value $D(q_m)$ at $q = q_m$ termed the (short-time) cage diffusion coefficient [see Fig. 8(b)]. As discussed earlier in relation to Eq. (7), deviations of $D(q)/D_0$ from the inverse, $1/S(q)$, of the structure factor are caused by HIs and reflected in values of the hydrodynamic function $H(q)$ different from 1. Akin to $S(q)$, the minimum of $H(q)$ is located at $q = 0$ and is equal to the sedimentation coefficient of a homogeneous monodisperse suspension in the linear response limit.[32] Note that the maximal deviation of $H(q)$ from 1 at $q = 0$, where $H(0) < 1$, is outweighed by the even smaller minimum of $S(q)$ at $q = 0$ [compressibility factor $S(0) < H(0)$], resulting in the distinct maximum $D(0) > D_0$ of $D(q)$ at $q = 0$, as seen in Fig. 9 and referred to as the collective diffusion coefficient.

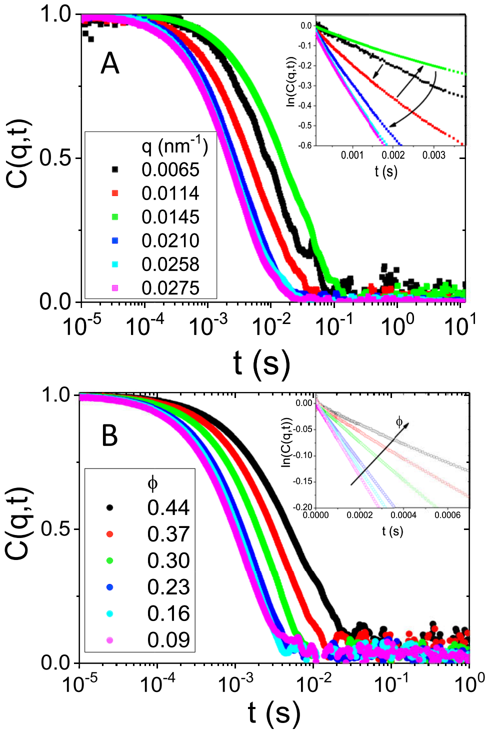

FIG. 8. (a) Normalized dynamic structure factor, $C(q, t)$, of *P2_126k* in the DCB-DE solvent mixture at different scattering wavenumbers as indicated, for $\phi = 0.44$. The principal peak of $S(q)$ is located here at $q_m = 0.0147$ nm^{-1}. Inset: The same data are shown in a log-lin plot to display more clearly the initial short-time decay according to Eq. (6). The arrows denote the nonmonotonic response of the dynamics around the peak of the structure factor. (b) $C(q, t)$ as a function of correlation time t for different volume fractions as indicated, at specific wavenumber $q = 0.027$ nm^{-1} located to the right of q_m where $S(q) \approx 1$ and where, approximately, the self-diffusion is probed. Inset: The same data are shown in a log-lin plot to display better the short-time decay. The arrow denotes the slowing down of the initial decay with increasing volume fraction.

Figure 9 includes our experimental results for the $D(q)$ of the considered core-shell particle systems (filled symbols), extracted from the initial slope of $C(q, t)$ determined using 3D-DLS (see Fig. 8). The q dependence of $D(q)$ becomes more pronounced with increasing volume fraction, reflecting the interplay of direct (thermodynamic) and hydrodynamic interactions described by Eq. (7). The solid and dashed lines are spherical annulus model predictions for $D(q; \gamma)$ with $\gamma = 1$ (impermeable hard spheres) and $\gamma = 0.95$ (moderately permeable hard spheres), respectively, using Eq. (14) for $H(q; \gamma)$ applicable for $qR_H \geq 2$, and the hard-sphere Percus-Yevick result[48] for $S(q)$ whose peak value $S(q_m)$ is for $\phi \leq 0.4$ close to Eq. (16). The q-dependent distinct part of the input $H(q; \gamma = 1)$ in Eq. (14) is calculated using the Beenakker-Mazur method (BM) method,[43] while the self-part input $D_S(\gamma)$ is obtained from Eq. (10).

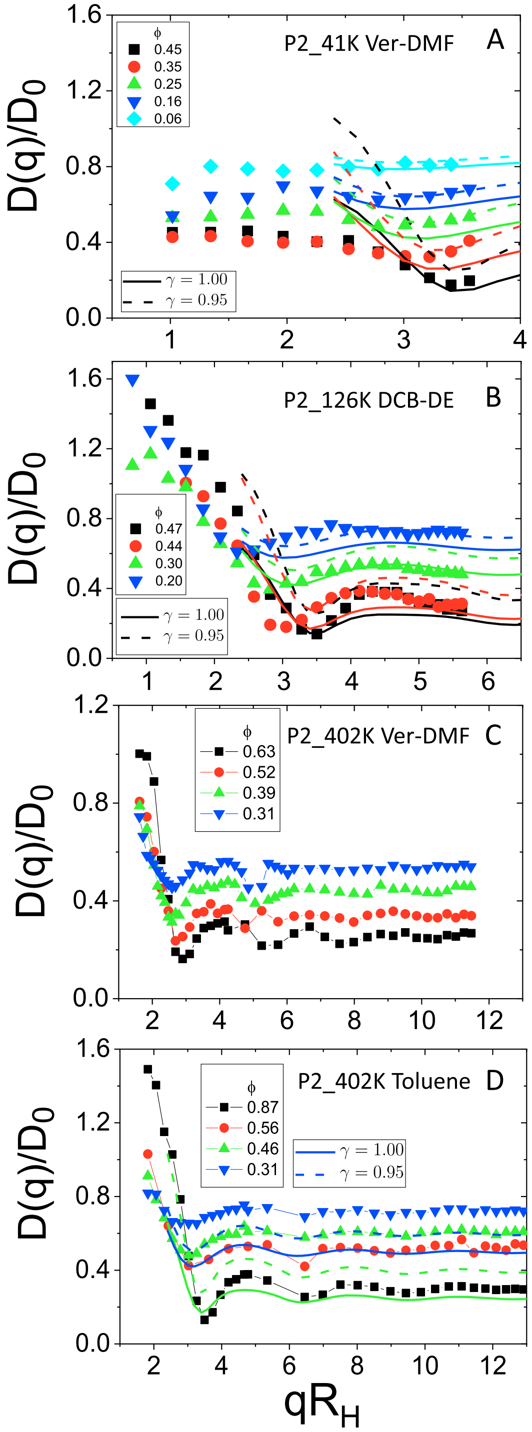

FIG. 9. 3D-DLS data (filled symbols) for the normalized diffusion function $D(q)/D_0$ as a function of qR_H, for systems (a) *P2_41k* in Veratrole-DMF, (b) *P2_126k* in DCB-DE, (c) *P2_402k* in veratrole-DMF, and (d) *P2_402k* in toluene at four different volume fractions as indicated. Solid lines in (a) and (b) are spherical annulus model predictions for $D(q)$ based on Eq. (14), using $\gamma = R_H/R_{eff} = 1$, while dashed lines are the spherical annulus prediction using $\gamma = 0.95$. Different colors label different volume fractions.

For the two larger-particle systems *P2_126k* and *P2_402k* in both solvents, the high qR_H regime is practically reached experimentally according to Figs. 9(b) and 9(c) since $S(q) \to 1$ and $D(q) \to D_S$ becomes q-independent and is equal to the self-diffusion coefficient D_S. The cage diffusion coefficient, $D(q_m)$, quantifying structural cage relaxation, and also D_S decrease with increasing volume fraction as expected from the enhanced HIs and $S(q_m)$ values. By contrast, $D(q)$ at small q increases with increasing ϕ, mainly triggered by the associated decrease in $S(q \ll q_m)$ [cf. Fig. 4 and $I_{conc}(q) \propto S(q)$]. Note, however, that for the larger *P2_402k* particle systems in Figs. 9(c) and 9(d), the experimental small-q range is limited to $qR_H \geq 1$ so that the true value for the collective diffusion coefficient $D_C = D(q \to 0)$ is not accessed. Regarding the smaller-particle system in Fig. 9(a), the variations in $D(q)$ are less pronounced than in the other two larger particles while the large-q plateau regime is not clearly reached experimentally. For comparison, Figs. 9(a), 9(b), and 9(d) include also the spherical annulus model predictions for impermeable hard spheres where $\gamma = 1$ (solid curves) and permeable hard spheres with $\gamma = 0.95$ (dashed curves), corresponding in the latter case according to Eq. (9) to a hydrodynamic permeation length $\sqrt{k}$ of 5% of the (effective) hard-core radius. Note that in using the spherical annulus model we prefer to limit the theoretical curves to nonsmall values around q_m or larger, as for $q \approx 0$, $D(q) \propto 1/S(q)$ is very sensitive to the form of the pair potential which for soft particles differs distinctly from the hard-sphere interactions underlying the spherical annulus model.

According to the model calculations, the hydrodynamic effect of solvent permeability is to enhance the reduced diffusion function $D(q;\gamma)/D_0(\gamma) \propto H(q;\gamma)$ and, in particular, more strongly for small q where the enhancement of the hydrodynamic function $H(q;\gamma)$ caused, in the case of permeable particles, by the weakened HIs is most pronounced.

For wavenumber values near to and larger than the principal structure factor peak position q_m, the experimental $D(q)$ in Fig. 9(a) for the smaller particles, *P2_41k*, is roughly located in between the two spherical annulus curves for impermeable and permeable hard spheres. For smaller q values, however, the $D(q)/D_0$ of the *P2_41k* system levels off practically rather than increasing toward values larger than one as predicted for (permeable) hard spheres. Judging from the concentration dependence of q_m depicted in Fig. 6, as expected, the *P2_41k* system behaves more hard-sphere-like than the other two core-shell systems, yet the concentration dependence of $S(q_m)$ and $S(0)$ is, according to Fig. 7, distinctly different (weaker) than that of hard spheres. The experimental values for $S(q \approx 0)$ at $\phi > 0.4$ are nearly concentration-independent and distinctly larger than the hard-sphere $S(0)$. This explains the small values of the experimental $D(q)$ in Fig. 9(a) at smaller wavenumbers. It should be noted that a similar finding of a rather weak, in comparison with hard spheres, minimum at q_m was reported for another core-shell particle system (silica-PDMS), likewise in the concentrated regime studied by two-color DLS.[4]

For the intermediately large *P2_126k* particle system of Fig. 9(b), the experimental $D(q)$ is underestimated to some extent by the impermeable hard-sphere prediction (blue, red, and black solid curves), except for $\phi = 0.3$ (green solid curve), albeit the overall shape of the diffusion function is well reproduced. For $q > q_m$, there is better agreement of the experimental data with the $D(q)$ curves for permeable hard spheres. The strongest deviations between the experiment and (permeable) hard-sphere predictions are observed at small q and at the minimum of $D(q)$ at q_m which grow with increasing volume fraction. That the largest deviations of experimental and spherical annulus $D(q)$'s are observed at small q is owed to the strong sensitivity of $S(0)$ to the softness and range of the direct interaction potential.

For the largest $P2\_402k$ particles in veratrole-DMF [Fig. 9(c)], the minimum of $D(q)$ is measured at rather low values, i.e., at $q_m R_H < 3$, in agreement with the position of the $S(q)$ maximum (see Figs. 5 and 6). As discussed above (Subsection IV B 1), this has been seen in other soft colloids, such as starlike micelles. However, it cannot be accounted for by any model with hard-core (solid or permeable) interactions. Therefore, we have not attempted to describe quantitatively the measured $D(q)$ of the larger and softer $P2\_402k$ particles in veratrole-DMF [Fig. 9(c)] using the spherical annulus model. Moreover, the analytic expressions of this simple model are not applicable to very large volume fractions near the overlap value. Hence, here we only show the experimental data. For $P2\_402k$ particles suspended in the veratrole-DMF mixture, a strong small-q decline of $D(q)$ is observed in Fig. 9(c). The locations of the local minima and maxima are in accord with those of the associated $1/S(q)$ in Fig. 5. The cage (or structural) diffusion coefficient $D(q_m)$, in particular, is accordingly located at smaller wavenumber values ($q_m R_H \approx 2.80$) than those for (permeable) hard spheres at the same volume fraction and than that for the smaller and less soft particles in Figs. 9(a) and 9(b). Consistent with the findings in Figs. 5 and 6, this is indicative of direct interactions that are longer-ranged than those of the $P2\_41k$ and $P2\_126k$ particles. Upon changing the solvent from veratrole-DMF to toluene [cf. Fig. 9(d)], the particles swell by about 12% and become softer. The minimum of $D(q)$ is consequently located at larger q_m values than those in the solvent mixture [Fig. 9(c)]. We can therefore attempt to fit the experimental $D(q)$ data for these large particles in toluene up to $\phi = 0.54$ with theoretical predictions for solid and permeable spheres [see Fig. 9(d)] with the same values of up to ϕ_{eff}. Note that while the $D(q)$ minimum is close to the one for HSs as seen in Fig. 6, it does not coincide with the position of $S(q)$ apparent maximum, which is evidently affected by a particle form factor that is changing with increasing volume fraction.

We analyze next the volume fraction dependence of the self-diffusion coefficient, D_S, extracted at the high q limit of the measured $D(q)$ where we expect to have $S(q) \to 1$. Figure 10 shows the experimental $D(qR_H \gg 1)/D_0 \approx D_S/D_0$ (solid symbols) as a function of ϕ_{eff}, for all considered core-shell systems. While the depicted data for the intermediate sized, $P2\_126k$, and large, $P2\_402k$, particles in both solvents are determined from the large-qR_H regime of DLS measurements, those for the smaller particles, $P2\_41k$, are taken for the largest attained q values where however the genuine large-q limit of $D(q)$ is not reached. As mentioned above, this plot was created after determining in a self-consistent way (in practice after one iteration) the value of γ and therefore the related $\phi_{eff} = \phi/\gamma^3$. Our experimental data are compared with the spherical annulus model predictions for the $D_S(\phi;\gamma)/D_0(\gamma)$ of solvent-permeable colloidal hard spheres according to Eq. (10), for fitting values of γ as indicated in the figure. We reemphasize that Eq. (10) describes well the high-precision hydrodynamic force multipole simulation (HYDROMULTIPOLE) data by Abade *et al.*[37,49–51] for (uniformly) permeable and spherical annulus particles, as shown, e.g., in a comprehensive study by Riest and Nägele.[10]

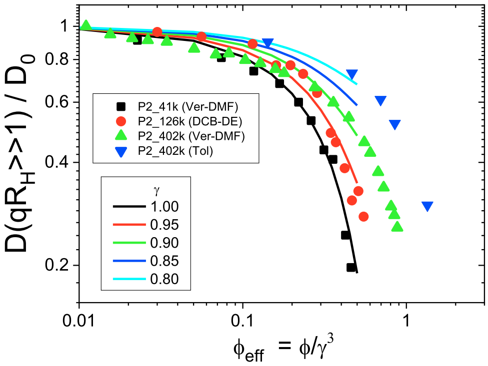

FIG. 10. Experimental estimates (solid filled symbols) of the normalized short-time self-diffusion coefficient, $D_S/D_0 \approx D(q \gg 1/R_H)/D_0$ as a function of effective volume fraction, for the considered core-shell systems as indicated. Solid lines are fits to the experimental data using the accurate spherical annulus model expression for D_S/D_0 given in Eq. (10), with fit values for $\gamma = R_H/R_{eff}$ listed in the figure legend. For $\gamma = 1$, the annulus model describes no-slip colloidal hard spheres.

Except for the data for the $P2\_41k$ particles (solid black squares) which follow the theoretical prediction for the short-time self-diffusion coefficient of impermeable hard spheres (black solid curve) rather closely even for large concentrations, for all the other core-shell systems the slowing down of D_S cannot be described quantitatively by the single-parameter spherical annulus model. The experimental D_S of the intermediately large particles $P2\_126k$ decreases in general slower than the smaller $P2\_41k$ particles and the impermeable hard sphere prediction ($\gamma = 1$). Its volume fraction dependence can follow rather well the permeable hard-sphere model using $\gamma = 0.95$, when the experimental data are plotted self-consistently as a function of the corresponding ϕ_{eff}. This suggests, according to Eq. (9), a mean hydrodynamic penetration depth of $\sqrt{k} \approx (1-\gamma)R_H/\gamma = 10.79$ nm.

For the larger and softer core-shell particles $P2\_402k$, experimental data of D_S are also compared with the theoretical predictions of the spherical annulus model in both solvents. The decay of D_S for the $P2\_402k$ particles in veratrole-DMF is more faster than in toluene when plotted as a function of concentration (or $\phi = c/c^*$), indicative of the softer character discussed above. Moreover, the decay of D_S in the $P2\_402k$ in veratrole-DMF seems more complex than in toluene, although there are less experimental points in the latter. When compared with the spherical annulus model predictions with $\gamma = 0.90$, we notice that experimental data (again plotted self-consistently vs the corresponding ϕ_{eff}) decrease stronger at small ϕ_{eff}, while roughly around $\phi_{eff} = 0.2$ they start to follow the permeable sphere model curve. For this system, $\gamma = 0.90$ corresponds to a mean hydrodynamic penetration depth $\sqrt{k} = 46.67$ nm, clearly larger than what was found for the smaller particles, $P2\_126k$.

The decay of D_S with increasing concentration is weaker for the large particle system in toluene. However, here, D_S cannot be fitted successfully if plotted in a self-consistent way vs ϕ_{eff}, by the spherical annulus model using any value γ. Here, experimental data are plotted vs ϕ_{eff} corresponding to $\gamma = 0.85$. For comparison, we show the model predictions both for $\gamma = 0.85$ (corresponding to a $\sqrt{k} = 117.5$ nm) and $\gamma = 0.80$ (corresponding to a $\sqrt{k} = 82.9$ nm). It is obvious that the experimental data for the larger and softer particles cannot be appropriately described by the spherical annulus model with $\gamma = 0.85$, as the latter predicts a much stronger decrease in D_S with the corresponding ϕ_{eff}. Moreover, even the model predictions with $\gamma = 0.8$ are slightly below the experimental data, which are however plotted as a function of the ϕ_{eff} of $\gamma = 0.85$; hence, if the proper ϕ_{eff} would have been used the experimental data would have been shifted even further to the right and thus not agree with the model. We can thus conclude that, as expected, the model reached its limitations and a more comprehensive theoretical approach would be needed, probably taking into account both softness and permeability effects.

While the precise origin for the more complex volume fraction dependence of D_S in veratrole-DMF is not fully understood, we may speculate that it is due to solvent-specific interactions that change with increasing concentration in the mixed solvent, as such a response is not observable in toluene. The latter is clearly a good solvent for the PMMA polymer grafted chains and actually a better one than the veratrole-DMF mixture, as suggested by the shell size, h, molecular weight dependence (Fig. 2, top) and the A_2 measurements [Fig. 3(b)]. The grafted polymer chains may thus undergo a conformation change above a certain concentration (still below c^*) caused by a preferential distribution of solvents within and around the particle or a change of solvent quality. An accompanied shrinkage of the polymer shell may therefore lead to the observed softening of the decrease in D_S within $\phi_{eff} = 0.1$–0.3. A similar but less pronounced might be expected for the *P*2_126*k* particles in the mixed solvent; however, the effect is not clear probably because the size of the polymer grafted layer is shorter and denser (as the grafting density is the same) and hence should not be affected as much (if at all) by any preferential solvent distribution. A similar plateau region in the volume fraction dependence of the self-diffusion coefficient was found also in block copolymer colloidal micelles with a cross-linked core[5] and was attributed, inspired by computer simulation predictions, to a solvent-mediated core shrinkage with increasing concentration.

We may now compare the hydrodynamic penetration depth, $\sqrt{k}$, which is a quantitative measure of the solvent permeable part of the particle for the different systems and solvents. While for the smaller particles, *P*2_41*k*, D_S essentially follows the nonpermeable hard sphere predictions (therefore $\sqrt{k} = 0$), for the intermediate particle, *P*2_126*k*, we get $\sqrt{k} = 10.79$ nm, and for *P*2_402*k* in veratrole-DMF, we similarly get $\sqrt{k} = 46.67$ nm. By contrast, the softer system, *P*2_402*k* in toluene, as discussed above (see also Fig. 10) cannot be fitted by the spherical annulus model.

In concluding our discussion of self-diffusion, we point out that while being quite small, D_S does not vanish at the glass transition volume fraction, which for monodisperse hard spheres occurs at $\phi \approx 0.58$. By contrast, the long-time (out-of-cage) self-diffusion coefficient D_L quantifying the long-time slope of the particle mean-squared displacement vanishes (practically) at the glass transition concentration, as the suspension viscosity diverges here.

According to Fig. 10, most D_S data points of the core-shell systems are located above the impermeable hard-sphere curve (solid black line). Since the hydrodynamic volume fraction is related with c/c^*, for sufficiently soft, deformable, or interpenetrable particles, a singular behavior of such dynamic quantities at a glass transition can take place for volume fractions larger than one, i.e., for $c > c^*$. This is indeed the case for a variety of soft colloid systems, polymeric microgels, multiarm starlike polymers, and micellar solutions.[6,9,15]

Softness and solvent permeability effects are also manifested in the (short-time) cage diffusion coefficient $D(q_m;\gamma) = D_0(\gamma)H(q_m;\gamma)/S(q_m)$ constituting the minimum of $D(q)$ and related to cooperative diffusion across a nearest neighbor pair distance $\sim 2\pi/q_m$. Experimental results for the reduced diffusion $D(q_m)/D_0$ of the current core-shell systems are shown in Fig. 11(a) in conjunction with the associated spherical annulus model fits of this quantity. Experimental data are again plotted as a function of ϕ_{eff} in order to be self-consistently compared with theoretical predictions as well as with D_s. Similarly with the latter, the cage diffusion coefficient slows

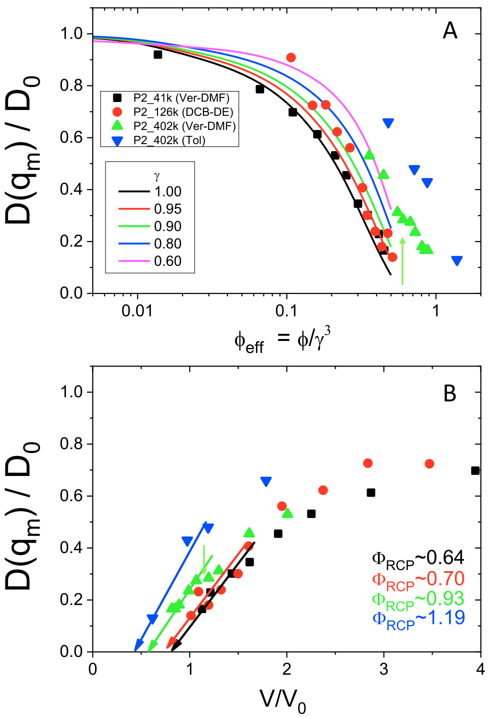

FIG. 11. (a) Normalized experimental cage diffusion coefficient $D(q_m)/D_0 = H(q_m)/S(q_m)$ (solid filled symbols) of all core-shell particles as a function of effective volume fraction, ϕ_{eff}, using the same γ values for each system as those for D_s in Fig. 10. Solid lines are spherical annulus model predictions based on Eqs. (14) and (15) for $H(q_m;\gamma)$ and Eq. (16) for the (effective) hard-sphere peak height $S(q_m)$, with different γ values as shown in the legend. (b) Cage diffusion coefficient plotted vs the reduced volume per particle $V/V_0 = \pi/6\phi$ following Segre *et al.*[47] The arrows denote the estimate of the RCP volume fraction ϕ_{RCP} where $D(q_m) = 0$, for all samples. With increasing particle softness, RCP increases from 0.64 for system *P*2_41*k* to the distinctly larger value of 1.19 for the *P*2_402*k* particles in toluene.

down with increasing volume fraction [Fig. 11(a)] with its decrease being stronger for the small and intermediate sized particles *P2_42k* and *P2_126k* and weaker for the large *P2_402k* particles suspended in veratrole-DMF and in even more in toluene. The volume-fraction dependence of the experimental $D(q_m)$ data is contrasted with the spherical annulus model predictions, based on Eqs. (14)–(16) (solid curves) with the same γ values as those used to describe D_S in Fig. 10.

Although for the two smaller particles *P2_42k* and *P2_126k* experimental data for the cage (structural) diffusion approach the theoretical predictions used in Fig. 10 to describe the self-diffusion, for the larger and softer particles the experimental cage diffusion decreases much slower than the annulus model predictions used to fit the self-diffusion (for comparison, $\gamma = 0.8$ and $\gamma = 0.6$ are shown). Note, however, that as discussed in Subsection III B, the employed spherical annulus model expression for $D(q_m)$ is less accurate than the one in Eq. (10) for D_S since the former tends to overestimate cage diffusion for $\gamma \lesssim 0.8$.

We point out that the $D(q_m)$ data for *P2_402k* in veratrole-DMF reveal a change of slope around $\phi_{eff} \approx 0.45$ [see vertical arrow in Fig. 11(a)], related to an associated change of slope in the self-diffusion coefficient as a function of ϕ_{eff} noted in Fig. 10 and a plateaulike region of $S(q_m)$ around the same volume fraction. Although, as discussed above, the form factor may change in this regime the fact that a similar behavior is also seen in $D(q)$s suggests that there is a real qualitative effect in this concentration regime. This behavior may originate from a retraction of the outer part of polymer grafted chains with increasing concentration and therefore an overall shrinkage of the particle which leads to a lower actual volume fraction. If there is arm retraction and overall particle shrinkage by increasing the volume fraction (as has been suggested in similar systems), then ϕ_{eff} does not take into account such a change; hence, the value of ϕ_{eff} is apparently overestimated.

In Fig. 11(b), we replot $D(q_m)$ as a function of the reduced free volume per particle, $V/V_0 = \pi/(6\phi)$, where $V_0 = (2R_H)^3$. Following Segre *et al.*[52] who performed such an analysis for colloidal hard spheres, this plot provides a means to estimate an apparent RCP volume fraction ϕ_{RCP} by an extrapolation to the free volume value where $D(q_m)$ becomes zero, indicating complete suppression of diffusional motion on the length scale set by q_m. Note that here we use the experimental, $\phi = c/c^*$, related with the measured hydrodynamic radius, R_H, in order to avoid any model dependent uncertainties for the estimation of the apparent RCP where $D(q_m)$ vanishes. Our experimental data at high volume fractions have a linear dependence on V/V_0 for associated small values of the latter. The RCP volume fraction estimates deduced from a linear extrapolation to $D(q_m) = 0$ are $\phi_{RCP} \approx 0.67$ for the small (and least soft) particles *P2_41k* in veratrole-DMF, $\phi_{RCP} \approx 0.70$ for the intermediately large and soft particles *P2_126k* in DCB-DE, while for the larger, softer, and more permeable particles distinctly larger volume fraction values $\phi_{RCP} \approx 0.91$ for *P2_402k* in veratrole-DMF and $\phi_{RCP} \approx 1.19$ for *P2_402k* in toluene are obtained. Note that volume fraction values larger than one for the random close packing are attainable since particles are soft, interpenetrable, and compressible.

We finally discuss the short-time collective diffusion coefficient $D(q \to 0)$ quantifying diffusional relaxation of long-wavelength concentration fluctuations by cooperative particle motion. For the larger particles (*P2_402k*) in both solvents, $D(q \to 0)$ cannot be safely extracted as our experimental wavenumber window is restricted to values $qR_H \gg 1$, while for the smaller, *P2_41k*, and intermediate, *P2_126k*, particles we used the $D(q)$ values measured at the lowest assessed q as a good estimate (i.e., lower bound) of the collective diffusion coefficient.

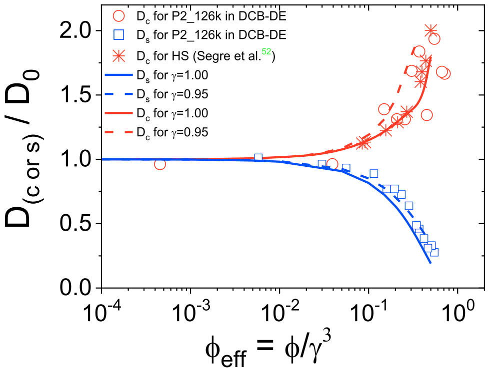

FIG. 12. Experimental estimates for the normalized collective diffusion coefficient $D_c/D_0 = H(0)/S(0)$ (open red circles) and normalized short-time self-diffusion coefficient D_S/D_0 (open blue squares) of the core-shell system *P2_126k* in DCB-DE as functions of ϕ_{eff}, extracted from the low-q and high-q data of $D(q)$, respectively. Red stars are experimental hard-sphere data for the collective diffusion coefficient D_c measured by Segre *et al.*[52] The red up-turning curves are the spherical annulus model results for the collective diffusion coefficient using Eq. (11) for $H(0;\gamma)$ and Eq. (17) for $S(0)$, while the blue down-turning curves are the spherical annulus model prediction for $D_S(\gamma)/D_0$ by Eq. (10). Depicted are the model curves for $\gamma = 1$ (solid) corresponding to no-slip (impermeable) hard spheres and $\gamma = 0.95$ (dashed) corresponding to solvent-permeable spheres with penetration length equal to five percent of the excluded volume radius.

In Fig. 12, we plot the collective short-time diffusion coefficient estimate, $D(q \ll q_m)$, together with self-diffusion coefficient data as a function of ϕ_{eff}, for the intermediate-sized particle system *P2_126k* in DCB-DE, for which both quantities can be safely determined. For comparison, we also show experimental data[52] for the collective diffusion of impermeable colloidal hard spheres (sterically stabilized PMMA particles), as well as the spherical annulus predictions for both $D_c = D(q = 0)$ and D_S using $\gamma = 1$ and 0.95, respectively. Note that the collective diffusion coefficient, D_c, increases with volume fraction, indicative of a suspension with predominantly repulsive interactions of shorter range, while D_S decreases which would be the case even for attractive interactions. While there is a significant scatter in the depicted $D_c = D(q = 0)$ data, owing to large errors in estimating the zero-q limit, qualitatively the collective diffusion data follow the impermeable hard-sphere behavior, whereas the experimental self-diffusion follows the spherical annulus curve for permeable particles.

V. CONCLUSIONS

The structure and short-time dynamics in concentrated suspensions of soft and semipermeable core-shell particles were measured in a wide range of volume fractions through 3D dynamic light scattering experiments. Various systems with different molecular weights of polymer grafted chains and different solvents were utilized to investigate the effects of softness and solvent permeability in the dynamics around the peak of the structure factor. The equilibrium microstructural properties show deviations from hard sphere behavior, indicating a soft character of the particles, and provide strong indications of a variation of the outer shell and shrinkage of the overall particle size with increasing concentration, a phenomenon that is solvent dependent and stronger for the larger and softer particle system (*P*2_402*k*). More specifically, while for the smaller particles the position q_m of the main structure factor peak follows the HS behavior, for the other two, larger, core-shell particles, longer-range repulsive interactions, not accounted for in the hydrodynamic radius, R_H (measured by DLS), are manifested by a shift of q_m to smaller values than what is expected in the case of hard spheres.

While it is difficult to extract the equilibrium static structure factor, $S(q)$, by 3D-SLS due to unaccountable concentration changes in the particle form factor, dynamic properties are accurately determined by 3D-DLS with the diffusion function, $D(q)$, deduced unambiguously from the correlation functions (or dynamic structure factor), $C(q, t)$. The latter exhibits, to a large extent, a single exponential relaxation decay for all samples and volume fractions measured. Therefore, the initial slope of $C(q, t)$ provides an accurate determination of the relaxation time, from which the diffusion function, $D(q)$, was extracted at different q.

The $D(q)$ was measured as a function of (hydrodynamic) volume fraction, $\phi = c/c^*$, for all particle/solvent systems, exhibiting a slowing down around the peak position of $S(q)$, as expected according to Eq. (7). The short-time diffusion coefficient, $D(q)$, was probed, in particular, at low wavenumbers [below the peak position of $S(q)$], yielding the collective diffusion coefficient, at the peak of $S(q)$ (at $q = q_m$) where cage (or structural) diffusion is monitored and in the high-q limit where self-diffusion is measured.

Experimental findings were also compared extensively with analytic theoretical results for $D(q)$ in the simple spherical annulus model, describing, in conjunction with Eq. (9) and $\phi_{eff} = \phi/\gamma^3$, solvent-permeable and impermeable colloidal hard spheres. As a first step, we directly confronted the shape of the experimental $D(q)$ with model predictions at high volume fractions in the liquid regime. Stronger quantitative discrepancies were revealed for the smaller (harder) particles at low q, where $D(q)$ is almost q independent, as well as for the larger particles in the mixed solvent (veratrole-DMF) where the minimum $D(q_m)$ is detected at far smaller q values than expected for permeable or impermeable HSs. In a more detailed comparison of experiments and theory, the spherical annulus model is found to describe overall well the concentration dependence of the (short-time) self-diffusion coefficient D_S, deduced experimentally as the high-q form of the experimental $D(q)$ for the two soft and permeable core-shell systems, i.e., *P*2_126*k* in DCB-DE and *P*2_402*k* in veratrole-DMF, utilizing as the only fitting parameter $\gamma = R_H/R_{eff}$, corresponding to an effective hard sphere radius R_{eff} or equivalently to a Darcy hydrodynamic penetration depth. More specifically, the self-diffusion coefficient for these two systems can be described well using $\gamma = 0.95$ and 0.9, respectively. On the other hand, for the particles with the shorter grafted chains (thus harder and less permeable), D_S follows well the nonpermeable hard-sphere prediction (with $\gamma = 1$), whereas the softer system, consisting of the large particles *P*2_402*k* in toluene, cannot be fitted with the spherical annulus model predictions, providing evidence of the limits of the model.

We have further determined experimentally the structural (or cage) diffusion coefficient, $D(q_m)$, as the minimum of $D(q)$, and an estimate, when possible at the low q limit, of the collective diffusion coefficient, D_C. A direct comparison with the spherical annulus model suggests that the experimental $D(q_m)$ data deviate stronger from the model predictions than the corresponding self-diffusion coefficient D_S; therefore, it can be considered a more sensitive probe of softness and permeability effects and consequently a more challenging dynamic quantity to be fitted by a comprehensive theory. For the collective diffusion coefficient, D_C, we note that the experimental estimate for the intermediate particle size system is in qualitative agreement with model predictions using the fitting parameter, $\gamma = 0.95$, that was found to describe well the volume fraction dependence of D_S. However, as mentioned above, the D_C for the small and hard particles clearly deviates from the model predictions (both the permeable and impermeable models), while for the large (and softer) particle systems the low-q limit of $D(q)$ is not adequately reached to allow for a reasonable estimation of D_C.

While the spherical annulus model appeals by its simplicity and the well-tested good accuracy of the analytic expression for $D(q)$ listed in Eqs. (10)–(17), all details of the soft interaction potential of core-shell particles are here lumped together into a single effective hard-core radius R_{eff} with associated effective volume fraction ϕ_{eff}. These details affect $D(q) = D_0 H(q)/S(q)$ not only explicitly via the inverse static factor $1/S(q)$, and here, in particular, at small q owing to an enlarged osmotic compressibility, but also implicitly by affecting the hydrodynamical factor $H(q)$ in Eq. (8) via the equilibrium configurational average. In using the spherical annulus model for the interpretation of experimental $D(q)$ data, one therefore attributes deviations from an effective hard-sphere behavior (once ϕ_{eff} has been defined) to solvent permeability, with a consequential system-dependent likelihood to overestimate the hydrodynamic particle permeability and its influence in comparison with particle softness and flexibility. Using instead of the spherical annulus model a refined theoretical analysis based on a more complex realistic pair potential will further require, for internal consistency, a detailed modeling of the hydrodynamic particle structure which strongly complicates the calculation of $D(q)$ for concentrated suspensions. Such an analysis requiring elaborate hydrodynamic simulations can be the subject of future work. In this context, we note that recent calculations of $D(q)/D_0$ for soft Hertz potential particles mimicking homogeneous, nonionic spherical microgel particles show a distinct small $-q$ downshift of $D(q)/D_0$ with increasing softness, while the oscillations at larger q are damped and $D(q)/D_0$ is slightly upshifted.[53] The softness effects on $D(q)$ described here are consistent with the experimental deviations of $D(q)/D_0$ in Fig. 9(b) from the spherical annulus model predictions where (dynamic) softness effects are disregarded.

Finally, from a zero-value extrapolation of the measured cage diffusion coefficient $D(q_m)$ as a function of the reduced free volume per particle (proportionally to $1/\phi$), we have estimated the random close packing (RCP) volume fraction for all considered core-shell systems. The deduced RCP volume fraction shows the expected increase with increasing particle softness, acquiring values close to that of hard spheres for the smaller and harder particle system ($\phi_{RCP} \approx 0.64$ for *P*2_41*k*) and clearly larger values than HS close-packing for the softer particle systems ($P2\_126k$ and $P2\_402k$) since outer shell shrinkage, polymer chain interpenetration, and deformation are possible.

SUPPLEMENTARY MATERIAL

See supplementary material for the experimental structure factors S(q) and the experimental estimates for the normalized diffusion coefficients (D_c or D_m or D_s) of the core-shell systems not shown in the main text.

ACKNOWLEDGMENTS

We acknowledge financial support from the Greek Secretariat for Research and Technology projects Aristeia "Microsoft" and Thales "Covisco." G.P. gratefully acknowledges support from the Humboldt Foundation and G.N. acknowledges support from the Deutsche Forschungsgemeinschaft (Grant No. SFB-985, Project No. B6).

REFERENCES

[1] P. Ahlrichs, R. Everaers, and B. Dünweg, Phys. Rev. E **64**, 040501(R) (2001).

[2] J. Stellbrink, J. Allgaier, and D. Richter, "Dynamics of star polymers: Evidence for a structural glass transition," Phys. Rev. E **56**, R3772 (1997).

[3] R. Sigel, S. Pispas, D. Vlassopoulos, N. Hadjichristidis, and G. Fytas, "Structural relaxation of dense suspensions of soft giant micelles," Phys. Rev. Lett. **83**, 4666 (1999).

[4] G. Petekidis, J. Gapinski, P. Seymour, J. S. van Duijneveldt, D. Vlassopoulos, and G. Fytas, "Dynamics of core-shell particles in concentrated suspensions," Phys. Rev. E **69**, 042401 (2004).

[5] B. Loppinet, G. Fytas, D. Vlassopoulos, C. N. Likos, G. Meier, and G. J. Liu, "Dynamics of dense suspensions of star-like micelles with responsive fixed cores," Macromol. Chem. Phys. **206**, 163–172 (2005).

[6] A. Pamvouxoglou, "Viscoelastic response of micelles with chemically cross-linked cores," B.S. thesis, University of Crete, 2006.

[7] T. Eckert and W. Richtering, "Thermodynamic and hydrodynamic interaction in concentrated microgel suspensions: Hard or soft sphere behavior?," J. Chem. Phys. **129**, 124902 (2008).

[8] J. Gapinski, A. Patkowski, A. J. Banchio, J. Buitenhuis, P. Holmqvist, M. P. Lettinga, G. Meier, and G. Nägele, "Structure and short-time dynamics in suspensions of charged silica spheres in the entire fluid regime," J. Chem. Phys. **130**, 084503 (2009).

[9] P. Voudouris, J. Choi, H. Dong, M. R. Bockstaller, K. Matyjaszewski, and G. Fytas, "Effect of shell architecture on the static and dynamic properties of polymer-coated particles in solution," Macromolecules **42**, 2721–2728 (2009).

[10] J. Riest, T. Eckert, W. Richtering, and G. Nägele, "Dynamics of suspensions of hydrodynamically structured particles: Analytic theory and applications to experiments," Soft Matter **11**, 2821–2843 (2015).

[11] I. Deike, M. Ballauff, N. Willenbacher, and A. Weiss, "Rheology of thermosensitive latex particles including the high-frequency limit," J. Rheol. **45**, 709–720 (2001).

[12] A. Le Grand and G. Petekidis, "Effects of particle softness on the rheology and yielding of colloidal glasses," Rheol. Acta **47**, 579–590 (2008).

[13] V. Carrier and G. Petekidis, "Nonlinear rheology of colloidal glasses of soft thermosensitive microgel particles," J. Rheol. **53**, 245 (2009).

[14] J. M. Brader, M. Siebenbürger, M. Ballauff, K. Reinheimer, M. Wilhelm, S. J. Frey, F. Weysser, and M. Fuchs, "Nonlinear response of dense colloidal suspensions under oscillatory shear: Mode-coupling theory and Fourier transform rheology experiments," Phys. Rev. E **82**, 061401 (2010).

[15] D. Vlassopoulos, G. Fytas, T. Pakula, and J. Roovers, "Multiarm star polymers dynamics," J. Phys.: Condens. Matter **13**, R855–R876 (2001).

[16] S. Gupta, M. Camargo, J. Stellbrink, J. Allgaier, A. Radulescu, P. Lindner, E. Zaccarelli, C. N. Likos, and D. Richter, "Dynamic phase diagram of soft nanocolloids," Nanoscale **7**, 13924–13934 (2015).

[17] A. J. Banchio and J. F. Brady, "Accelerated Stokesian dynamics: Brownian motion," J. Chem. Phys. **118**, 10323–10332 (2003).

[18] P. N. Pusey and R. J. A. Tough, "Particle interactions," in *Dynamic Light Scattering*, edited by R. Pecora (Plenum, New York, 1985).

[19] W. van Megen and S. Underwood, "Dynamic light scattering study of glasses of colloidal hard spheres," Phys. Rev. E **47**, 248 (1993).

[20] A. J. Banchio and G. Nägele, "Short-time transport properties in dense suspensions: From neutral to charge-stabilized colloidal spheres," J. Chem. Phys. **128**, 104903 (2008).

[21] A. J. Banchio, M. Heinen, P. Holmqvist, and G. Nägele, "Short- and long-time time diffusion and dynamic scaling in suspensions of charged colloidal particles," J. Chem. Phys. **148**, 134902 (2018).

[22] P. Holmqvist, P. S. Mohanty, G. Nägele, P. Schurtenberger, and M. Heinen, "Structure and dynamics of loosely cross-linked ionic microgel dispersions in the fluid regime," Phys. Rev. Lett. **109**, 048302 (2012).

[23] M. Imai, M. Kurimoto, F. Matsuura, Y. Sakuma, and T. Kawakatsu, "Diffusion of surfactant micelles in fluid and crystal phases," Soft Matter **8**, 9892–9905 (2012).

[24] K. Ohno, T. Morinaga, K. Koh, Y. Tsujii, and T. Fukuda, Macromolecules **38**, 2137–2142 (2005).

[25] M. Daoud and J. Cotton, "Star shaped polymers: A model for the conformation and it's concentration dependence," J. Phys. **43**, 531–538 (1982).

[26] C. Urban and P. Schurtenberger, "Dynamic light scattering in turbid suspensions: An application of different cross-correlation experiments," in *Trends in Colloid and Interface Science* (Springer, 1998), Vol. XII, pp. 61–65.

[27] K. Schätzel, "Suppression of multiple scattering by photon cross-correlation techniques," J. Mod. Opt. **38**, 1849–1865 (1991).

[28] C. Urban and P. Schurtenberger, "Characterization of turbid colloidal suspensions using light scattering techniques combined with cross-correlation methods," J. Colloid Interface Sci. **207**, 150–158 (1998).

[29] C. Urban, L. Gauckler, P. Schurtenberger, and H. J. Watzke, Development of fiber optic based dynamic light scattering for a characterization of turbid suspension, cERN Document Server (Switzerland) ER, 2005, http://cdsweb.cern.ch/oai2d.py.

[30] E. Overbeck, C. Sinn, and T. Palberg, "Approaching the limits of multiple scattering decorrelation: 3D light-scattering apparatus utilizing semiconductor lasers," in *Optical Methods and Physics of Colloidal Dispersions* (Springer, 1997), pp. 117–120.

[31] L. B. Aberle, P. Hülstede, S. Wiegand, W. Schröer, and W. Staude, "Effective suppression of multiply scattered light in static and dynamic light scattering," Appl. Opt. **37**, 6511–6524 (1998).

[32] G. Nägele, Phys. Rep. **272**, 215–372 (1996).

[33] G. C. Abade, B. Cichocki, M. L. Ekiel-Jezewska, G. Nägele, and E. Wajnryb, "High-frequency viscosity of concentrated porous particles suspensions," J. Chem. Phys. **133**, 084906 (2010).

[34] B. Cichocki, M. L. Ekiel-Jezewska, and E. Wajnnryb, J. Chem. Phys. **140**, 164902 (2014).

[35] P. Debye and A. M. Bueche, J. Chem. Phys. **16**, 573 (1948).

[36] G. C. Abade, B. Cichocki, M. L. Ekiel-Jezewska, G. Nägele, and E. Wajnryb, "Diffusion, sedimentation, and rheology of concentrated suspensions of core-shell particles," J. Chem. Phys. **136**, 104902 (2012).

[37] G. C. Abade, B. Cichocki, M. L. Ekiel-Jezewska, G. Nägele, and E. Wajnryb, "Short-time dynamics of permeable particles in concentrated suspensions," J. Chem. Phys. **132**, 014503–014517 (2010).

[38] A. J. Banchio, G. Nägele, and J. Bergenholtz, J. Chem. Phys. **113**, 3381 (2000).

[39] J.-P. Hansen and L. Verlet, "Phase transitions of the Lennard-Jones system," Phys. Rev. **184**, 151–161 (1969).

[40] G. Nägele, M. Kollmann, R. Pesche, and A. J. Banchio, Mol. Phys. **100**, 2921–2933 (2002).

[41] A. Donev, F. H. Stillinger, and S. Torquato, "Unexpected density fluctuations in jammed disordered sphere packings," Phys. Rev. Lett. **95**, 090604 (2005).

[42] R. Kurita and E. R. Weeks, "Experimental study of random-close-packed colloidal particles," Phys. Rev. E **82**, 011403 (2010).
[43] C. Beenakker and P. Mazur, "Diffusion of spheres in a concentrated suspension II," Physica A **126**, 349–370 (1984).
[44] S. Forster, A. Timmann, M. Konrad, C. Schellbach, A. Meyer, S. S. Funari, P. Mulvaney, and R. Knott, "Scattering curves of ordered mesoscopic materials," J. Phys. Chem. B **109**, 1347–1360 (2005).
[45] B. J. Berne and R. Pecora, *Dynamic Light Scattering: With Applications to Chemistry, Biology, and Physics* (Dover Books on Physics, 2003).
[46] M. Laurati, J. Stellbrink, R. Lund, L. Willner, E. Zaccarelli, and D. Richter, "Asymmetric poly(ethylene-alt-propylene)-poly(ethylene oxide) micelles: A system with starlike morphology and interactions," Phys. Rev. E **76**, 041503 (2007).
[47] P. N. Segre, S. P. Meeker, P. N. Pusey, and W. C. K. Poon, "Viscosity and structural relaxation in suspensions of hard-sphere colloids," Phys. Rev. Lett. **75**, 958 (1995).
[48] L. Verlet and J.-J. Weiss, Phys. Rev. A **5**, 939 (1972).
[49] G. C. Abade, B. Cichocki, M. L. Ekiel-Jezewska, G. Nägele, and E. Wajnryb, "Dynamics of permeable particles in concentrated suspensions," Phys. Rev. E **81**, 020404(R) (2010).
[50] B. Cichocki, M. L. Ekiel-Jezewska, G. Nägele, and E. Wajnryb, "First-order virial expansion of short-time diffusion and sedimentation coefficients of permeable particles suspensions," Phys. Fluids **23**, 083303 (2011).
[51] G. C. Abade, B. Cichocki, M. L. Ekiel-Jezewska, G. Nägele, and E. Wajnryb, "Rotational and translational self-diffusion in concentrated suspensions of permeable particles," J. Chem. Phys. **134**, 244903–244907 (2011).
[52] P. N. Segre, O. P. Behrend, and P. N. Pusey, "Short-time Brownian motion in colloidal suspensions: Experiment and simulation," Phys. Rev. E **52**, 5070–5083 (1995).
[53] J. Riest, M. Brito, and G. Nägele, "Dynamic properties of soft Hertzian particles suspensions" (unpublished).